KØBENHAVNS UNIVERSITET
DET NATUR- OG BIOVIDENSKABELIGE FAKULTET

Measuring the quantum dot induced phase shift of light transmitted through a nanophotonic waveguide

M.Sc. Thesis by:

Mathias Jakob Rønne Staunstrup

Supervised by:

Hanna Le Jeannic
Nir Rotenberg
Peter Lodahl

UNIVERSITY OF COPENHAGEN

Name of institute: Niels Bohr Instituttet

Department: Quantum Photonics

Author: Mathias Jakob Rønne Staunstrup

Hand in date: 15/04/2020

KU-id: jrh351

E-mail: jrh351@alumni.ku.dk

Title: Measuring the quantum dot induced phase shift of light transmitted through a nanophotonic waveguide

Abstract

This thesis explores the transmission of light through a nanophotonic waveguide with an embedded single solid state quantum dot. The coupling between the quantum dot and the waveguide gives rise to giant nonlinerarites at the single photon or weak coherent limit of the transmitted light. Focus is here put on the phase shift that light obtains after transmission of the quantum dot and waveguide system. The theory of transmission is explored for both for an istotropic and chiral coupling of the quantum dot to the waveguide. These configurations give rise to respectively a $\pi/2$ and π phase shift. Theory shows that especially chiral coupling is shown to be more robust to physical dependent factors and supplies even larger nonlinearity than isotropic coupling. For the measurement of this phase shift, a Mach-Zehnder interferomter was constructed as a new tool for the lab. Methods have been developed to stabilize the interferometer, in order to compensate for large mechanical fluctuations in the interferometric signal. Using this interferometer, the spectral response of the phase shift induced by an isotropic coupled quantum dot is measured. For this first direct measurement of the phase shift, a maximum phase shift of $58.5^o \pm 0.3^o$ is measured. The spectral response showed good agreement with theory. Finally, a measurement of the power dependence of the phase shift is performed, and show nonlinear behavior as predicted in the theory.

Acknowledgements

First, I want to thank Hanna Le Jeannic for the invaluable help throughout every step of the project, and of course for always being a nice and friendly person. Next I want to thank Alexey Tiranov for helping realize the results later on in the project. I Also want to thank Nir Rotenberg for introducing me to the project and the initial theory, as well as the nice weekly meetings. The Hy-q and quantum Photonics group have been an extremely friendly and open group to work in, to this I want thank Peter Lodahl for allowing me to participate actively in the group and at events. Furthermore, I want to thank Nils Hauff and Vasiliki Angelopoulou for additional help with theory and laboratory work.

Last but not least, I want to thank my office mates Arianne, Carlos and Simon for keeping the spirit high.

Contents

Chapter 1

Introduction

one of the current challenges in quantum optics is building circuits of light and quantum emitters,in order to utilize the quantum nature of particles for both quantum computational-and communication applications. The complete advancement would potentially allow, quantum cryptation for communication that would disallow eavesdropping of shared information or. With regards to computing, the complexity of some classical algorithms can be lowered, thereby shortening computational duration from even longer than a human life span to a reasonable amount of time [31]. In addition, it could also be used for simulations of the quantum dynamics of systems that are otherwise too complex to be simulated on a classical computer, such as chemical reactions, and thus gain information that could potentially help in other fields of science[10]. These circuits could either be realized in large freespace optical setup or in smaller integrated photonic circuits Photonic circuits have in the recent years shown promise for the scaleability of quantum computing due to well-developed fabrication methods. Circuits on either Silicon or Semiconductor chips[30], consist of many sub elements such as input/output gratings that allow the coupling to free space laboratory light. These gratings couple to waveguides that can be used to for example to route photons on the chip, and perform either linear operation, but also nonlinear for example through the interactions with embedded quantum emitters. The focus in this thesis is to work with on semiconductor quantum dots consisting of InAs that are situated in a waveguide made of GaAs. Recognized for their ability to produce single photons[33], another important feature is how the quantum dot emitter can interact with light that is propagating in the waveguide.

Upon interaction with an emitter, not only the intensity of transmission is altered, but a phase shift will also be gained. Such a phase shift is a nonlinear operation that is sensitive to single photons, enable moreover the QD as a new tool in quantum circuitry.

Depending on the type of waveguide, the emission of the quantum dot can be tailored. This will effect the QD interaction and can then enhance the phaseshift

up to a maximum phase shift of π, without any photon lost in the process[25].

Additionally the phase shift will depend on a range of physical parameters describing the QD and waveguide field system. Measuring the phase shift will then not only give proof its existence but could also be used for characterization of the emitter waveguide system. Here we set out to do a first direct measurement of the phase shift on light transmitted through a nanophotonic waveguide with an embedded quantum dot.

In Chapter 2 the phase shift operation will be introduced, as well as the QD-waveguide system on which we will be working.

In Chapter 3 We will derive the theory of light transmitted through a waveguide with a coupled single emitter. Especially, we will explore two different waveguide configurations with either isotropic or chiral emission. With focus on the dependency of physical parameters.

In Chapter 4 The experimental set for measuring the phase shift with a Mach-Zehnder interferometer is presented. Due to large fluctuations in the interferometer signal, methods is here developed to stabilize the interferometer for phaseshift measurements.

Finally in chapter 5, a first direct measurement of a quantum dot induced phaseshift will be presented and compared to theory. We will also present its nonlinear dependence with power.

Chapter 2

Phase shifts induced by wave guide embedded quantum dots

2.1 Few photon dependent phase shift

2.1.1 Overview

For the application of using light in communications systems the ideal case is to use light on the few photon level. At the few photon level we can also get into the space of quantum mechanical effects. This might be used to realize quantum computation-and communications tasks. In this sense one might think of photons as flying qubits to which we are able to encode and read information[20]. However to do that, interactions on the few photon scale needs to employed. This renders the need for a substitute for linear optical media and high power nonlinear media. The solution is giant nonlinearities i.e. nonlinearities sensitive to the single photon level. To obtain these giant non linearity quantum emitters can be used. The quantum emitters could for example be atoms, ions, molecules or quantum dots[8][23].
So far most experiments have concentrated on measuring the nonlinear behavior by observing the transmission through the system for increasing power[5][47]. However, the interaction also induces a phase shift on the transmitted light. The phase shift might be system dependent and thus utilized in different ways.

2.1.2 Application in quantum computing and communication

Setting up the interaction between light and matter in structured manners in so called circuits, allows for different types of quantum operations to be applied. These

complete operations constitutes of a set of subsequent quantum gate operations [31]. The over arching goal is thus to realize this entire set of operations for general use. Quantum operations have been implemented in a variety of different systems. In atomic ensembles, entanglement for teleportation have been presented [36]. In a photonical setting a controlled phase shift gate has been introduced using cross phase modulation with nonlinear Kerr material [9].

Circuits that are realized in using freespace optics will take an increasingly bigger size for larger circuits and will end up taking too much space with high instability and fluctuations. In contrast, the photonic setting allows small and complex integrated circuits to be fabricated directly on sample. Waveguides guiding light can be fabricated like wires directly on sample. This allows for the propagation of light in between on sample structures such as resonators and beamsplitters[30][22]. For instance a circuit in silicon photoic have shown the realization of a CNOT gate and quantum entanglement[35][22]. Introducing nonlinear behavior into such photonic circuits allows for the introduction of additional interactions at the single photon level[34][23]

Here we shall consider the nonlinearity in terms of a single quantum dot emitter. This QD coupled to a nanophotonic crystal waveguide[24]. Depending on the wave guide type and quantum dot coupling, the light transmitted through the waveguide will either perfectly reflected or transmitted. In addition, a phase of respectively $\pi/2$ and π is obtained. The latter case is of chiral behavior. These situations are true at the single photon level, but for higher the effect might only be partial or completely gone for strong ligth[25][47].

Combining multiple waveguides could make up circuits of light and emitters. Arranging circuits in specific ways could shape the photon state and mediate distanced interactions with quantum dots for using in networks[6][23]. Especially the chiral transmission is of high interest due to the obtainable phase shift of π. We could here imagine the use of the chiral interaction situated in one arm of a Mach-Zehnder interferometer. This configuration could be used as single photon diode and with the control of the quantum dot transition as a CNOT gate. The realization of these elements could provide great use future circuits for quantum computing and information in quantum networks[28] [44]. Measuring the phase shift through such a waveguide system might help characterization and further give proof of its existence.

2.1.3 Current status on measuring few photon phase shift

Measuring the phase shift induced by a single emitter is an experiment of fundamental interaction between light an matter. Thus previous measurements of the phase shift have been of interest in a range of fields.

Some phase shift measurement have been carried out with ions and ensembles of atoms. By measuring with a trapped RB^{87} ion in one arm of a Mach-Zehnder interferometer a phase shift up to 1^o[1]. Another experiment [40] measured on RB^{85} strongly coupled to a cavity an emitter induced phased shift of 140^o using homodyne detection. A similar experiment but on caesium vapor have shown up to around 30^o phase shift including the cavity system [46].

Another experiment on trapped Ytterbium ions have shown up to 2^o phase shift[12].

An atomic ensemble of rubidium atoms were found to enhance the index of refraction on resonance, thus inducing a phase shift up 7π for the transmitted light.[51]. Conditional non-linear phase shift have been observed on the single photon level due to electromagnetic induced trasparency [11].

In addition to measurement on ensembles and single atoms experiments have been made on organic molecules. Here a maximum phase shift up to 6^o is measured using homodyne detection [37].

Here we shall focus on the interaction with semi conductor quantum dots. Though consisting of many atoms they can behave like single emitters[24]. Enabling the measurement of the phase shift of light interacting with these quantum emitters, will both be able to help tell whether the phase shift is possible and in what regime of environment depending parameters is limiting.

Some phase shift induced by quantum dot have already been experimentally measured for quantum dots in cavitys. In micropillar cavities, phase shift of around 2.8^o [50] and 80^o [49] have been observed.

In another cavity system, consisting of a photonic crystal defect cavity. Phase shift have been measured up to $\pi/4$ [14].

In this thesis we shall consider QD embedded in nanopohtonic wave guides. With interest on the phase shift obtained for ligth transmitted through such a wave guide. One such measurement have been done and inferred a 40^o from correlation measurent on the transmitted light.[21]. Here we shall examine the possibility of measuring the phase shift in a direct manner using an interferometric method.

2.2 Quantum dots in nanophotonic wave guides

2.2.1 Quantum dots

The quantum dots considered in this thesis is small semiconductor crystals made of InAs. They consist approximately 10^5 atoms and have a size of tens of nanometers[24]. They are situated in a much bigger millimeter scaled crystal of GaAs which is also a semiconductor, as sketched on Fig.2.1. The electron movement in such a crystal follow the typical band structure for periodical arranged atoms in condensed matter[42]. Such semi conductor materials can undergo excitation through optical light between the valence and conduction band, at the direct bandgap. Upon excitation an electron can move to the conduction band while leaving a hole behind in the valence band. Such electron hole pair is also called an exciton. The electron will seek to be positioned at the lowest energy in conduction band, and the same is true for the hole in the valence band. Compared to GaAs, the direct bandgap energy of InAs is respectively higher and lower for the valence and conduction band (Fig.2.1). Thus forming a energy well that confine the exciton to the InAs quantum dot, in all spatial dimensions[24].

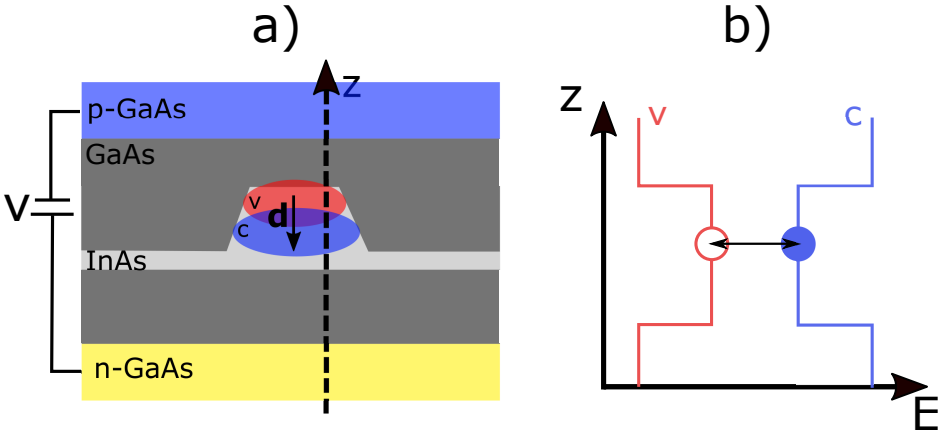

Figure 2.1: a) A schematic type picture of how the InAs QD is embedded inside a bigger GaAs diode. b) The corresponding simplified bandgap energy corresponding to the z-cut axis on the schematic

Due to the strong confinement, a simplified two band picure has shown sufficient for describing the physics of the exciton in the QD. This ultimately renders the comparable to a TLS. The quantum state of the electron or hole is spatially confined to the QD potential by an envelope function. This envelope for the conduction and valence has also been been drawn onto the schematic in Fig.2.1 as blue and red areas. Referencing respectively to the conduction(c) and valence band(v).

The difference between the average electron/hole position in the conduction/valence band effectively make up the emitter with a dipole $\boldsymbol{d}$.

The quantum dot might then be modeled like a single emitter two level system(TLS). With ground state$|g\rangle$ and excited state $|e\rangle$, as also sketched on Fig. 2.2

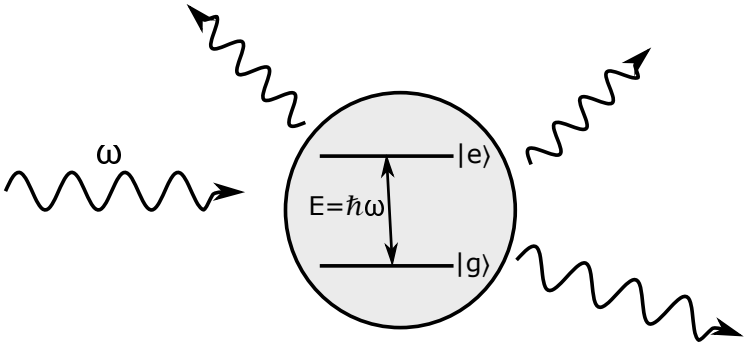

Figure 2.2: The schematic of a free emitting two level system with ground-and excited state $|g\rangle$ and $|e\rangle$. Excited by the incoming light of frequency ω, here comparable to the emitter energy E.

The TLS have the ability to be excited by light at resonance with the TLS transition. At relaxation the TLS reemit to the environment with a certain emission rate. Since the quantum dot is situated inside a crystal it is therefore in close connection to its environment. This leads to different environmental impacts on the QD, and thus how it interacts and emit light.

2.2.2 Environmental factors

Both the electron and hole will due to their charge be subject to a force from external fields. Thereby a field would effectively change both the energy potential of the exciton and the dipole vector. Thus free charges in the environment is a source of noise on the exciton. This noise effectively does a smearing of the TLS that result in spectral diffusion. This a type of spectral diffusion might be modelled as a spectral Gaussian noise [21].
Furthermore, this also renders the quantum dot tune able by applying an external constant electric field. That is why the sample in this case has been made as diode by with a positive(p-GaAs)-and negative(n-GaAs) doped GaAs around the intrinsic crystal where the quantum dot is situated, as indicated on Fig.2.1. The ability to tune the quantum dot will be used later experimentally by tuning in and out of resonance with a light field. The diode also reduce influence from free charge noise

on the sample by allowing a current to run[33].

In crystals temperature is manifested as vibrations called phonons dispersing through the material. This also apply for the sample crystal in this experiment. Elastic interactions between the emitter and the present phonon bath, introduces a broadening of the quantum dot emission rate. The interaction is much faster than the emitter decay rate and thus constitute a pure dephasing. Effectively it corresponds to a smearing of the energy levels in the TLS (Fig. 2.3).

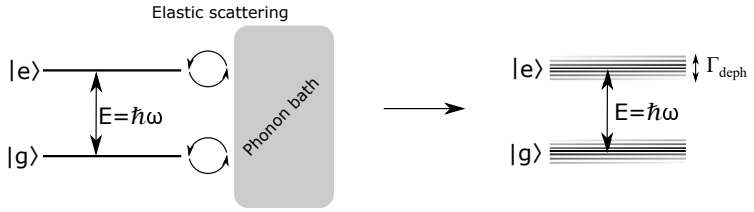

Figure 2.3: Smearing of the energy states of TLS due to elastic scattering with a phonon bath.

To reduce the broadening from phonons, the sample is situated in a cryostat where it is cooled to approximately 4 Kelvin. Using that the quantum dots is embedded in a in a larger crystal photonic structures can be used to guide the light field for interaction.

2.2.3 Guiding light

Photonic structures can be used to shape the light field and thus the QD emission and interaction. Here the ability to fabricate photonic structures on the sample using lithographic methods and etching of material[30] is used. With these photonic structures we can shape the local electric fields at the quantum dot position, which ultimately will change how its emitting into to the environment. This has been shown for quantum dots in both photonic crystals [26] and cavities[16]. In general the physics of how a dipole emitter radiate into the environment can be describe by the Greens tensor $\boldsymbol{G}$, which is an environmental dependent tool that can that can describe what the electric field $\boldsymbol{E}(\boldsymbol{r})$ at position $\boldsymbol{r}$ emitted from a point dipole $\boldsymbol{P}(\boldsymbol{r_0})$ at position $\boldsymbol{r_0}$. According to the relation

$$\boldsymbol{E}(\boldsymbol{r}) = \omega^2 \mu \mu_0 \boldsymbol{G}(\boldsymbol{r}, \boldsymbol{r_0}) \boldsymbol{P}(\boldsymbol{r_0}) \tag{2.1}$$

Where ω is the radial frequency of the electric field and μ_0 and μ are the vacuum- and relative material permeability[32]. To shape the emission we thus need to change

the emitter environment. This will take effect through the Greens tensor $\boldsymbol{G}$. Here we shall examine the case of nanophotonic crystal waveguides.

2.2.4 Nanophotonic crystal waveguides

Nanophotonic wave guides have the ability to confine and direct light, to increase interaction with embedded an embedded quantum dot.

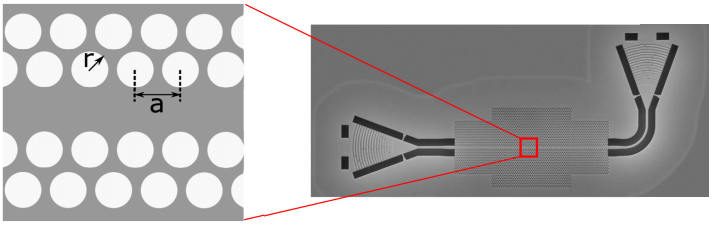

Figure 2.4: Schematic of a photonic crystal waveguide (PCW) to a corresponding area shown by red lines on a picture of a PCW made by a scanning electron microscope.

The nanophotonic waveguides we consider here are mad with nanophotonic crystals. The photonic crystal consist of regular triangular lattice structure, that has a crystal constant a that is around 250nm. The crystal is constructed by periodical removal of material on the sample in the shape of circular holes. This makes it a crystal consisting of the sample material(GaAs) and the surrounding environment (air/vacuum) that fills the holes. The holes have a radii of approximately 70nm. The wave guide is created by removing one row of holes from this entire crystal, as also shown in Fig.2.4. The waveguide is coupled to free space modes via input/output grating couplers situated in boths ends of the PCW.
Such a photonic crystal waveguide (PCW) can confine the light to the size of the gap, and thus interact well with Quantum dot emitter. The PCW limits the light modes to certain bands. On the edge of these bands, the local density of optical states is greatly enhanced[26]. The QD emission can then be highly edited in contrast to emission in bulk/free space.

2.2.5 QD coupling to wave guide modes

In bulk the, emitter may emit into all spatial modes with out any strong preference. However, wave guides encourages light to emit into modes that goes along with the wave guide direction. The effective emission from a quantum dot into wave guide

is defined from as a ratio between the total rate of emission and the portion that is emitted to wave guide modes.

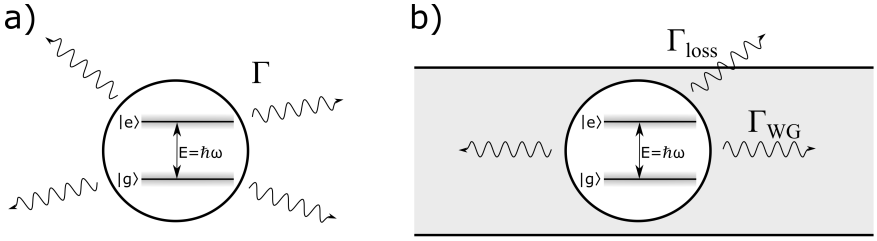

Figure 2.5: *a)* Free TLS emitting to all modes with rate Γ. *b)* Waeguide embedded TLS emitting into the waveguide with rate Γ_{WG} and out with loss rate Γ_{loss}.

This ratio is called the beta factor and is defined as

$$\beta = \frac{\Gamma_{WG}}{\Gamma_{WG} + \Gamma_{Loss}} \tag{2.2}$$

Where the total emission rate(denominator) consist of the emission rate to the waveguide Γ_{WG} and the rate of emission into non waveguide modes i.e. loss. These type of nanophotonic waveguides have shown high β-factors of close to 90%[21] up to 98% [2]. As considered earlier the dephasing has an broadening effect on the quantum dot. It is therefore preferable to have quantum freqeuncy be close to that of the PCW. Here the rate emission is enhanced and thereby the dephasing is minimized compared to the natural linewidth. In the group, similar QD waveguide systems have shown that the dephasing rate is of no major effect to the quantumdot broadening and the spectral linewidth and is thus limited to spontaneous emission[45][33][21], typical dephasing rates is found to be in a typical range of 0% to 2% of the natural emitter linewidth[21][13].

Quantum dots positioned in such wave guides have shown a good configuration for the production of single photons by resonantly exciting the quantum dot and letting it re-emit. The single photons from this have shown indistinguishabilty above 95% [48]. Rendering the setup a good candidate as a single photon generator in photonic circuits aswell.

2.2.6 QD interaction with the wave guide field

The interaction between a dipole emitter and optical electric field can in quantum mechanics be described via the Jaynes-Cummings model. The interacting Hamiltonian term between field and emitter provides $\hat{H}_{int} = -\hat{d} \cdot \hat{E}$. It is here evident that the interaction must be highly dependent on the polarization of the dipole and

electric field. In the case of the PCW the light polarization within the waveguide is mostly linear and thus only interact with linear dipole transitions. However a waveguide with circular polarized light can be made. It is similar to the one considered in Fig. 2.4, but the an asymmetry constant as shown in Fig.2.6 has been applied. The asymmetry is made by displacing the crystal by half a crystal period, thus called a glide plane waveguide (GPW).

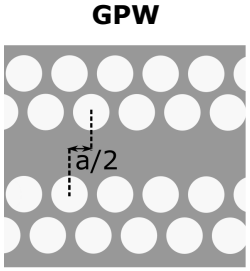

Figure 2.6: The schematic of the crystal structure in a glide plane waveguide

In the GPW structure the light is circular polarized and thus couple to circular dipole transitions in the QD. This is sketched for both wave guide configurations in Fig.2.7. The maximum obtainable phaseshift in these waveguide configurations are $\pi/2$ and π, for the PCW and GPW respectively. This is a case of respectively a isotropic(PCW) and chiral(GPW) wave guide coupling. Due to the π phaseshift only being obtainable in one transmission direction.
The circular polarization is what gives rise to the case of chiral interaction, due the difference in overlap between the dipole and light field in the different direction of propagation[44][25].

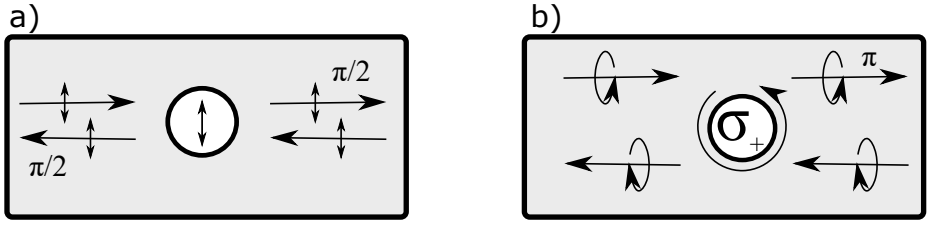

Figure 2.7: *a)* Transmission at linear dipole coupling in a PCW is isotropic *b)* Transmission for circular dipole coupling in a GPW is chiral.

2.2.7 Phase shift on light transmitted through a waveguide

Here we set out to measure the phase shift for light that is transmitted through a nanophotonic wave guide with an embedded quantum dot. The phase Will be mea-

sured through the interferometric difference between transmitted and freely propagating light, as schematized in Fig.2.8.

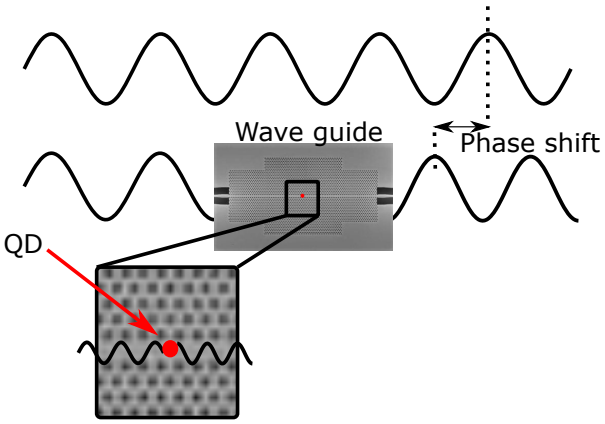

Figure 2.8: Schematic comparison between freely propagating light and QD wave guide system. Wave guide is the grey scale inset SEM picture with QD shown as *red* dot

Fig.2.8. [25]

However in order to know what to expect in the experiment, a theory has to be developed. Both for the case of isotropic coupling but also for chiral transmission.

Chapter 3

Theoretical description the emitter interaction in a wave guide.

In this section we will look at the mathematical modelling of a quantum dot embedded in a one dimensional waveguide. The theory is in large part inspired by reference [47] and [43]. We will here focus on the transmission of the light field, and its dependency on: the coupling β, the light intensity and dephasing rate of the QD.

3.1 Definition of the transmission

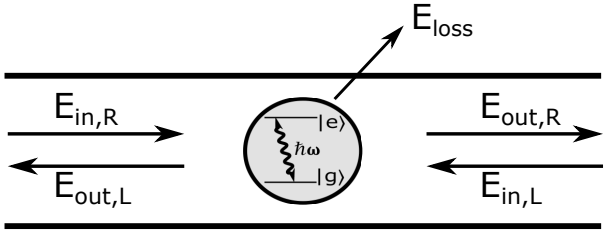

Figure 3.1: Simplified picture of a 1D waveguide containing an embedded TLS with an excited state $|e\rangle$ and a ground state $|g\rangle$ separated by the energy difference $\hbar\omega$. The arrows indicate the direction of propagation left(L) and right(R). The fields are defined before (in) and after (out) scattering. The loss is defined as non waveguide propagating modes

We define a transmission coefficient t that characterize the effect of the system on an input field. We can write the equation

$$E_{out,(L,R)} = t_{(L,R)} E_{in,(L,R)} \quad \longrightarrow \quad t_{(L,R)} = \frac{E_{out,(L,R)}}{E_{in,(L,R)}}$$

By differing between the direction of propagation left(L) and right(R), the directionality of the transmission may be taken into account. This will allow to account for the chiral coupling where the transmission is directional dependent.

Our goal is now to find the expectation values of the electric field operators, by modelling the interaction between the emitter and the light field.

3.1.1 Quantization of the electric field

To describe the electric field operators we first quantize the electromagnetic field by defining the creation $\hat{f}^\dagger$ and annihilation $\hat{f}$ operators of the bosonic photon field. They can be described by the Fock states $|n\rangle$, where n is the photon number:

$$\hat{f} = \sum_n \sqrt{n}\, |n-1\rangle \langle n|$$

$$\hat{f}^\dagger = \sum_n \sqrt{n+1}\, |n-1\rangle \langle n|$$

The operators follow the commutation relations, which can be written:.

$$[\hat{f}_k(\boldsymbol{r},\omega), \hat{f}^\dagger_{k'}(\boldsymbol{r}',\omega')] = \delta(\boldsymbol{r}-\boldsymbol{r}')\delta(\omega-\omega')\delta_{k,k'}$$

$$[\hat{f}_k(\boldsymbol{r},\omega), \hat{f}_{k'}(\boldsymbol{r}',\omega')] = 0$$

when taking into account the spatial position $\boldsymbol{r}$, frequency ω and the momentum k of the field excitation.
This can be used to define the known expression for the electric field operator in media[7].

$$\hat{E}^+(\mathbf{r},\omega) = i\mu_0\omega^2\sqrt{\frac{\hbar\epsilon_0}{\pi}} \int d\mathbf{r}' \sqrt{\epsilon_I(\mathbf{r}',\omega)}\mathbf{G}(\mathbf{r},\mathbf{r}',\omega) \sum_k \hat{f}_k(\mathbf{r}',\omega) \tag{3.1}$$

G is the Green tensor as described in Eq.2.1 in previous chapter. ϵ_0 is the vacuum permitivity and ϵ_I is the imaginary part of the material permitivity. The total electric field operator is $\hat{E} = \hat{E}^+ + \hat{E}^-$, where $\hat{E}^-$ is the hermitian conjugate of $\hat{E}^+$.

3.1.2 Electric field dynamics

The environment geometry and material is assumed overtime constant ie. $\dot{\boldsymbol{G}} = 0$ and $\dot{\epsilon_I} = 0$. Thereby only the evolution of the bosonic operator have to be considered. The evolution of the electric field is found using the Heisenberg equation:

$$\dot{\hat{f}}_k(\boldsymbol{r}, \omega) = \frac{i}{\hbar}[\hat{H}_s, \hat{f}_k(\boldsymbol{r}, \omega)]$$

$\hat{H}_s$ is the system Hamiltonian, which takes into account the field energy, the emitter energy and their interaction. The emitter is modeled by a excited state $|e\rangle$ and ground state $|g\rangle$ of energy E_e and E_g. We define using this, the atomic transition operators:

$$\hat{\sigma}_{eg} = |e\rangle \langle g| \qquad \hat{\sigma}_{ge} = |g\rangle \langle e|$$

The Hamiltonian describing coupling between a two level system and light field can be described by the Jaynes-Cumming model [15]:

$$\hat{H}_s = \hbar\omega_0 \hat{\sigma}_{eg}\hat{\sigma}_{ge} + \sum_k \int d\boldsymbol{r} \int d\omega \quad \hbar\omega \left(\hat{f}_k^\dagger(\boldsymbol{r}, \omega)\hat{f}_k(\boldsymbol{r}, \omega)\right) - \hat{\boldsymbol{d}} \cdot \hat{\boldsymbol{E}} \tag{3.2}$$

That in the first term contains the energy of the emitter. The second is the total photon energy and the last term is the interaction term between the emitter and electric field. Where $\hat{\boldsymbol{d}}$ is the dipole operator, defined in the case of a TLS as $\hat{\boldsymbol{d}} = \boldsymbol{d}\hat{\sigma}_{ge} + \boldsymbol{d}^*\hat{\sigma}_{eg}$. By inserting the electric field operator and the dipole operator into the interaction term, we obtain the last term to be:

$$\hat{H}_{int} = (\boldsymbol{d}\hat{\sigma}_{ge} + \boldsymbol{d}^*\hat{\sigma}_{eg})(\hat{E}^+ + \hat{E}^-)$$

The evolution of the electric field and atomic operators can be written as respectively:

$$\hat{\boldsymbol{E}}^+(t) = \hat{\boldsymbol{E}}^+(0)e^{i\omega_p t}$$

$$\hat{\sigma}_{eg}(t) = \hat{\sigma}_{eg}(0)e^{-i\omega_a t}$$

After substituting this into $\hat{H}_{int}$ we can apply the *rotating wave approximation*. Which allows the simplification:

$$\hat{H}_{int} = \boldsymbol{d}\hat{\sigma}_{ge}\hat{\boldsymbol{E}}^+ + \boldsymbol{d}^*\hat{\sigma}_{eg}\hat{\boldsymbol{E}}^-$$

Using this in the total system Hamiltonian we can now find the dynamics of the bosonic operator. Expanding the commutator in the Heisenberg equation we can write:

$$\dot{\hat{f}}_k(\boldsymbol{r},\omega) = \frac{i}{\hbar}(\hat{H}_s\hat{f}_k(\boldsymbol{r},\omega) - \hat{f}_k(\boldsymbol{r},\omega)H_s)$$

By using the commutation relation of the bosonic operators, and the fact that the bosonic operators commute with the atomic operators, we obtain the equation of motion:

$$\dot{\hat{f}}_k(\boldsymbol{r},\omega) = -i\omega\hat{f}_k(\boldsymbol{r},\omega) + \boldsymbol{d}^*\hat{\sigma}_{ge}i\mu_0\omega^2\sqrt{\frac{\epsilon_0}{\hbar\pi}}\int d\mathbf{r}'\sqrt{\epsilon_I(\mathbf{r}',\omega)}\mathbf{G}^*(\mathbf{r},\mathbf{r}',\omega)$$

This differential equation is solved by formal integration from an initial time t' to t. I addition we assume the emitter to be a point dipole at position $\boldsymbol{r}_a$. Using this we can write:

$$\hat{f}_k(\boldsymbol{r},\omega,t) = \hat{f}_k(\boldsymbol{r},\omega,t')e^{-i\omega(t-t')} + \mu_0\omega\sqrt{\frac{\epsilon_0}{\hbar\pi}}\sqrt{\epsilon_I(\mathbf{r},\omega)}\mathbf{G}^*(\mathbf{r}_a,\mathbf{r},\omega)\boldsymbol{d}^*(\boldsymbol{r_a})\int_{t'}^{t} dt'\hat{\sigma}_{eg}(t')e^{-i\omega(t-t')}$$

Using this in the electric field operator Eq.3.1, we obtain a total operator with two terms: one corresponding to the freely propagating electric field and the other to the scattered field of the quantum dot.

$$\hat{\boldsymbol{E}}^+ = \hat{\boldsymbol{E}}^+_{free} + \hat{\boldsymbol{E}}^+_{scat}$$

The last scattering term can be written as:

$$\hat{\boldsymbol{E}}^+_{scat} = i\mu_0^2\omega^4\frac{\epsilon_0}{\pi}\int d\boldsymbol{r}'\epsilon_I(\mathbf{r}')\mathbf{G}(\mathbf{r},\mathbf{r}',\omega)\mathbf{G}^*(\mathbf{r}',\mathbf{r}_a,\omega)\boldsymbol{d}^*(\boldsymbol{r_a})\int_{t'}^{t} dt'\hat{\sigma}_{eg}(t')e^{-i\omega(t-t')}$$

By using Greens tensor identity:

$$\mu_0\epsilon_0\omega^2\int d\boldsymbol{r}''\epsilon_I(\mathbf{r}'')\boldsymbol{G}(\boldsymbol{r},\boldsymbol{r}'',\omega)\boldsymbol{G}^*(\boldsymbol{r}'',\boldsymbol{r}',\omega) = \mathrm{Im}[\boldsymbol{G}^*(\boldsymbol{r},\boldsymbol{r}',\omega)]$$

we get

$$\hat{\boldsymbol{E}}^+_{scat} = i\mu_0\omega^2\frac{1}{\pi}\mathrm{Im}[\boldsymbol{G}^*(\boldsymbol{r},\boldsymbol{r}_a,\omega)]\boldsymbol{d}^*(\boldsymbol{r_a})\int_{t'}^{t} dt'\hat{\sigma}_{eg}(t')e^{-i\omega(t-t')}$$

We take here all the frequency components into account by integration, and inset the slowly varying atomic operator $\hat{\sigma}(t) = \tilde{\sigma}(t)e^{i\omega_a t}$. This leads to:

$$\hat{\boldsymbol{E}}^+_{scat} = i\mu_0\frac{1}{\pi}\int_0^\infty d\omega\omega^2\mathrm{Im}[\boldsymbol{G}(\boldsymbol{r},\boldsymbol{r}_a,\omega)]\boldsymbol{d}^*(\boldsymbol{r_a})\int_{t'}^{t} dt'\hat{\sigma}_{eg}(t')e^{-i(\omega-\omega_a)(t-t')}$$

Finally by using the Markoff approximation. This assumes that the atomic operator doesn't evolve during the interaction ie. $\hat{\sigma}(t) = \hat{\sigma}(t')$. The integral evaluates to

$$\hat{\boldsymbol{E}}^{+}_{scat}(\boldsymbol{r}, t) = i\mu_0 \frac{1}{\pi} \omega_a^2 \boldsymbol{G}(\boldsymbol{r}, \boldsymbol{r}_a, \omega_a) \boldsymbol{d^*}(\boldsymbol{r_a}) \hat{\sigma}_{eg}(t)$$

We can express this in terms of the freely propagating field $\hat{\boldsymbol{E}}^{+}_{free}(\boldsymbol{r}, t)$

$$\hat{\boldsymbol{E}}^{+}_{scat}(\boldsymbol{r}, t) = i\mu_0 \omega_a^2 \frac{\hat{\boldsymbol{E}}^{+}_{free}(\boldsymbol{r}, t) \boldsymbol{dG}(\boldsymbol{r}, \boldsymbol{r}_a, \omega_a) \boldsymbol{d^*}(\boldsymbol{r_a}) \hat{\sigma}_{eg}(t)}{\hbar \hat{\Omega}} \tag{3.3}$$

Where the Rabi frequency $\hat{\Omega} = \hat{\boldsymbol{E}}^{+}_{free}(\boldsymbol{r}, t)\boldsymbol{d}/\hbar$ is introduced. We furthermore define the dipole projected Greens tensor

$$g_{ij}(\boldsymbol{r}_i, \boldsymbol{r}_j) = \frac{i\mu_0 \omega_a^2}{\hbar} \boldsymbol{dG}(\boldsymbol{r}_i, \boldsymbol{r}_j, \omega_a) \boldsymbol{d^*}(\boldsymbol{r_a})$$

It describes the field propagation between point $\boldsymbol{r_i}$ and $\boldsymbol{r_i}$. The dipole projected Greens tensor for a simple 1D waveguide return a function and can be expressed as [4].

$$g_{ij}(\boldsymbol{r}_i, \boldsymbol{r}_j) = i\frac{\Gamma\beta}{2} e^{i_k |\boldsymbol{r}_i - \boldsymbol{r}_j|}$$

Here Γ_{wg} is the total emission rate of the emitter to waveguide modes and β is the coupling efficiency defined as $\beta = \Gamma_{wg}/(\Gamma_{wg} + \Gamma_{\text{loss}})$. Γ_{loss} is the emission rate into other modes than the waveguide and is thus lost, see Fig.3.2. This equation assumes a isotropic system and thus an equal rate emission into both directions left and right of the waveguide, hence the division of the factor 2. To expand this to the case of chiral coupling where we have need to differ between the direction of propagation. We define the chiral dipole projected Green function:

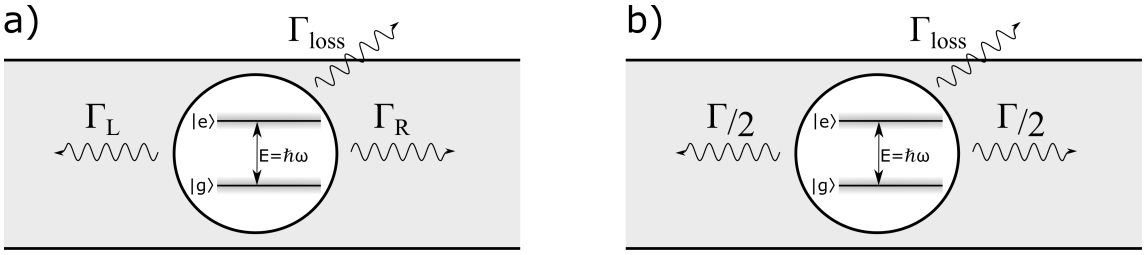

Figure 3.2: QD emitter embedded in a waveguide. a) Chiral coupling with directional emission rates Γ_L and Γ_R. b) Isotropic coupling with emission $\Gamma/2$. In both cases Γ_{loss} is the emission rate into non guided modes.

$$g_{ij}(\boldsymbol{r}_i, \boldsymbol{r}_j) = \Theta(\boldsymbol{r}_i - \boldsymbol{r}_j) i\Gamma\beta_L e^{i_k|\boldsymbol{r}_i - \boldsymbol{r}_j|} + \Theta(\boldsymbol{r}_i - \boldsymbol{r}_j) i\Gamma\beta_R e^{i_k|\boldsymbol{r}_i - \boldsymbol{r}_j|} \tag{3.4}$$

Where L, R is the direction of propagation of the light and thus the chiral coupled emission rate $\Gamma_{L,R}$ into said directions, as on Fig.3.2. Left and right propagation is defined with regards the position $\boldsymbol{r}_i$ as L when $\boldsymbol{r}_i < \boldsymbol{r}_j$, and R for the opposite sign. The Heaviside function Θ is introduced to select the correctly coupled term depending on the propagation direction.
The chiral coupling can defined as $\beta_{L,R} = \Gamma_{L,R}/(\Gamma_L + \Gamma_R + \Gamma_{\text{loss}})$, where we can see that we come back to the isotropic case if emission rate $\Gamma_L \neq \Gamma_R = \Gamma/2$ as also shown on Fig. 3.2.

With these results, we are finally able to calculate the transmission parameter as sought for in the beginning. We note that a freely propagating field will just be equal to that of the input field ie. $E_{free} = E_{in}$. Using this we obtain the equation for the transmission coefficient.

$$t_{L,R} = \frac{\langle \hat{\boldsymbol{E}}^+_{in,(L,R)} \rangle + \langle \hat{\boldsymbol{E}}^+_{Scat} \rangle}{\langle \hat{\boldsymbol{E}}^+_{in,(L,R)} \rangle}$$

Using the result for the scattered field Eq. 3.3. The coefficient equation reduces to.

$$t_{L,R} = 1 + \frac{g_{ij}(\boldsymbol{r}_i, \boldsymbol{r}_j)}{\Omega} \langle \hat{\sigma}_{ge}(t) \rangle \tag{3.5}$$

The term $e^{ik|r_i - r_j|}$ has been removed since it is an overall propagating phase that both the scattered and freely propagating light obtains in the waveguide.

We can see that all the input field terms cancel and we are left with to find an expression for the expectation value of the atomic transition operator. To find this, we must consider the dynamics of the emitter.

3.2 The emitter dynamics

The emitter system can be described by the density matrix defined as:

$$\hat{\rho} = \sum_{i,j} \rho_{ij} |i\rangle \langle j|$$

Where the elements $\rho_{i,j}$ for $i, j \in \{e, g\}$ describes the emitter population for $i = j$ and the system coherence for i. We can write the density matrix explicitly as:

$$\hat{\rho} = \begin{pmatrix} \rho_{gg} & \rho_{ge} \\ \rho_{eg} & \rho_{ee} \end{pmatrix}$$

From this we can obtain the expectation value of the atomic operator, needed to calculate the transmission coefficient in Eq. 3.5: It is obtained by:

$$\langle \hat{\sigma}_{i,j} \rangle = \mathrm{Tr}[\hat{\rho}\hat{\sigma}_{ij}] = \rho_{ji}$$

Since our emitter system is not isolated from a nearby environment it will suffer from decoherence, due to the elastic scattering of phonons in the environment, as mentioned in the previous chapter with relation to the puredephasing rate. This is modeled as a coupling to a reservoir. The reservoir is said to be big ie. unchanged and untangled with the emitter. Furthermore, it is assumed to be of much faster dynamics. The equation of motion for an emitter system coupled to this reservoir can be modeled by the Lindblad master equation [29]:

$$\dot{\hat{\rho}} = \frac{-i}{\hbar}[\hat{H}_s, \hat{\rho}] + \sum_{i,j} \frac{\Gamma_{ij}}{2}(2\hat{\sigma}_{ji}\hat{\rho}\hat{\sigma}_{ij} - \hat{\sigma}_{ii}\hat{\rho} - \hat{\rho}\hat{\sigma}_{ii}) \tag{3.6}$$

Terms where $i \neq j$ corresponds to atomic transitions and thus the rate of light emission. The rate is hereafter defined as $\Gamma_{eg} = \Gamma$. Terms for $i = j$ corresponds to transitions for state back to itself again. This effect introduces the loss of coherence for the emitter without an atomic transition, and correspond to the pure dephasing rate $\Gamma_{ee} = \Gamma_{gg} = \Gamma_{deph}$.
Since we are interested in the dynamics of the emitter we turn to consider the system in a rotating frame with the frequency ω_p of the photon field, which we consider constant. Since we assumed a constant driving we can turn to a semiclassical expression and remove the electric field operators, by introducing the Rabi frequency scalar $\Omega = \boldsymbol{d} \cdot \boldsymbol{E}^+/\hbar$. We obtain the Hamiltonian in photon frame as:

$$\hat{H}'_s = -\hbar\Delta\hat{\sigma}_{eg}\hat{\sigma}_{ge} + \hbar\omega_p \sum_k \int d\boldsymbol{r} \left(\hat{f}_k^\dagger(\boldsymbol{r}, \omega_p)\hat{f}_k(\boldsymbol{r}, \omega_p) \right) - \hbar\Omega(\hat{\sigma}_{ge} + \hat{\sigma}_{eg})$$

(3.7)

Δ is the detuning between the optical field and the emitter resonance and is defined as $\Delta = \omega_p - \omega_a$. Using this along with the Lindblad equation Eq.3.6, we obtain the equation of motion:

$$\dot{\rho}_{ge} = -(\Gamma_2 + i\Delta)\rho_{ge} + i\Omega(\rho_{ee} - \rho_{gg})$$

$$\dot{\rho}_{ee} = i\Omega(\rho_{eg} - \rho_{ge}) + \Gamma\rho_{ee}$$

Here we have defined $\Gamma_2 = \Gamma/2 + \Gamma_{deph}$. As we will be working under continuous wave excitation in the experiment, we can assume the operators in steady state ie. $\dot{\rho}_{ge} = \dot{\rho}_{ee} = 0$. Finally we obtain the elements of the density matrix as:

$$\rho_{ge} = -\frac{\Omega(\Gamma_2 + \Delta)}{\Gamma_2^2 + \Delta^2 + 4(\Gamma_2/\Gamma)\Omega^2} \tag{3.8a}$$

$$\rho_{ee} = -\frac{2\Gamma_2\Omega^2}{\Gamma(\Gamma_2^2 + \Delta^2 + 4(\Gamma_2/\Gamma)\Omega^2)} \tag{3.8b}$$

The other matrix elements can be obtained through $\rho_{eg} = \rho_{eg}^*$ and $\rho_{gg} = \rho_{ee}^*$. Using this in the next section we can obtain an expression for the coefficient of transmission in Eq.3.5.

3.3 Evaluating the transmission coefficent

Using the result for the density matrix elements Eq.3.8 and the expression for Eq.3.4 Along with $\langle\hat{\sigma}_{ge}\rangle = \mathrm{Tr}[\rho\hat{\sigma}_{ge}] = \rho_{eg}$. We calculate the transmission coefficient Eq.3.5. For respectively the chiral and isotropic case we obtain:

$$t = 1 + i\Gamma\frac{\beta}{2}\frac{i\Gamma_2 + \Delta}{\Gamma_2^2 + \Delta^2 + 4(\Gamma_2/\Gamma)\Omega^2} \tag{3.9}$$

$$t_{L,R} = 1 + i\Gamma\beta_{L,R}\frac{i\Gamma_2 + \Delta}{\Gamma_2^2 + \Delta^2 + 4(\Gamma_2/\Gamma)\Omega^2} \tag{3.10}$$

From theses final expressions we can calculate the expected phase shift of the transmitted light as the argument of the transmission coefficient. With this we can evaluate the phase shift dependence on dephasing Γ_{deph} , the coupling β and the power through the Rabi frequency Ω.

3.3.1 Intensity of transmission

Other than the transmission coefficient we also want to consider the intensity of the transmitted field as this is what, that is actually measured on the detector. The Transmission intensity can be written as

$$T = \frac{\langle\hat{E}^-\hat{E}^+\rangle}{\langle\hat{E}_{in}^-\hat{E}_{in}^+\rangle}$$

Following the same procedure as for the transmission coefficient we obtain the transmission intensities for respectively the isotropic and chiral case.

$$T = 1 - \frac{\beta\Gamma_2\Gamma(2-\beta)}{2(\Gamma_2^2 + \Delta^2 + 4(\Gamma_2/\Gamma)\Omega^2)} \tag{3.11}$$

$$T_{L,R} = 1 + \frac{2\Gamma_2\Gamma\beta_{L,R}(\beta_{L,R}-1)}{\Gamma_2^2 + \Delta^2 + 4(\Gamma_2/\Gamma)\Omega^2} \tag{3.12}$$

We now have the expressions to compare the spectral response of the transmission intensity and phase shift of the chiral and isotropic coupling. Displayed in Fig. 3.3 we consider the spectral response to the phase shift and transmission intensity for: zero dephasing, low power and ideal coupling of $\beta = 1$ and $\beta_{L,R} = 1$.

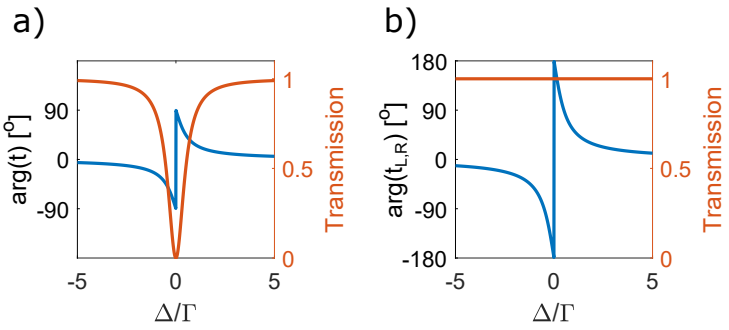

Figure 3.3: The phaseshift and transmission at $\Gamma_{deph} = 0$ and $\Omega = 0$ for a) isotropic coupling at $\beta = 1$. b) chiral coupling at $\beta_{L,R} = 1$

The isotropic coupling shows a lorentzians shaped response that goes to zero at resonance. Whereas the chiral coupling introduces unit transmission at all detuning. This would ultimately mean that in the full chiral case we would not measure any response on the intensity and all the effect would be in the phase shift. This argues for the experimental availability of being able to measure phase shifts, as a tool of characterization. We observe the expected maximum phase shift of 90^o for isotropic coupling and 180^o in the chiral case.

3.3.2 Saturation of Phase shift

Here we shall examine the power dependency of the phase shift. This is done through the Rabi frequency which is proportional to the electric field and thus proportional to the square root of the power. With regards to expression of transmission coefficient in Eq.3.9 and 3.10 the dependency is expected to be non linear. In Fig. 3.4 the spectral response of the phase shift for a range of powers in both the isotropic and chiral case is plotted.

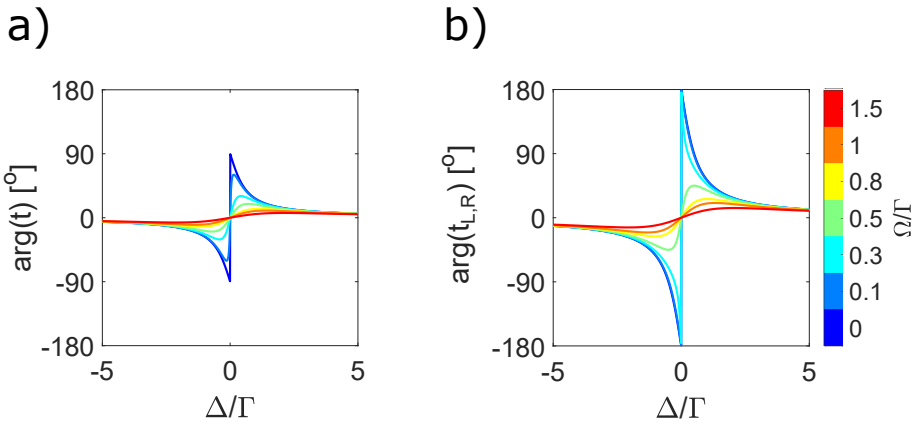

Figure 3.4: The spectral response of the phase shift for different Rabi frequencies, as indicated on the colorbar. For the isotropic (a)) and the chiral (b)) case.

The chiral case seems to be more robust for increasing power. To investigate further, the maximum phase is plotted as a function of the Rabi frequency for a range in Fig. 3.5.

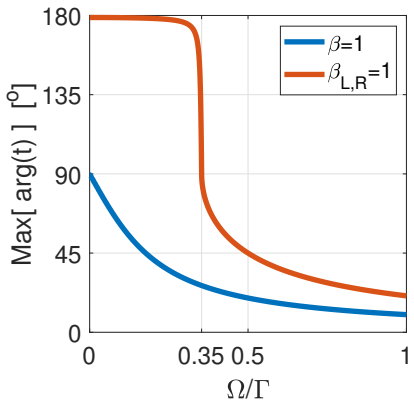

Figure 3.5: The maximum phase shift as a function of the Rabi frequency, for the isotropic (blue) and the chiral (orange) case.

The power dependence is highly non-linear for both cases. However, especially for the chiral case that seem to have a stable plateau of 180^o phase shift until a sharp point at $\Omega \sim 0.35\Gamma$ where the maximum phase shift drops from 180^o to 90^o. After this point it follows a similar behaviour to the isotropic case. This plateu gives some rest that the chiral π phase shift is robust.

3.3.3 Effect of the coupling

It is use full to see how the robustness as found in Fig: 3.5 depends of the coupling. As we in a real setup, wont have unit coupling. In Fig. 3.6 a) and b) the maximum phase shift has been plotted for the isotropic and chiral coupling case. When decreasing the isotropic coupling the maximum obtainable phase seems to directly decrease for decreasing β factor. While we in the chiral, the robustness plateau continues to exist until $\beta_{L,R}$ goes towards 0.5 where it reduces to the result of unit isotropic coupling. To observe the evolution of the sharp transition from the plateau, we define the point χ at which the largest absolute gradient of the maximum phase shift as function of power.
In Fig. 3.6.c) the χ point is plotted as a function of the coupling $\beta_{L,R}$. We observe here an almost linear correlation for high coupling and then a gradual increasing change when going towards $\beta_{L,R} = 0.5$. The measurement of this χ point might then be a direct method to obtain the coupling for chiral systems.

3.3.4 Effect of the dephasing

In a similar as when considering the power dependency, the effect that dephasing has on the phase shift is considered in Fig. 3.7

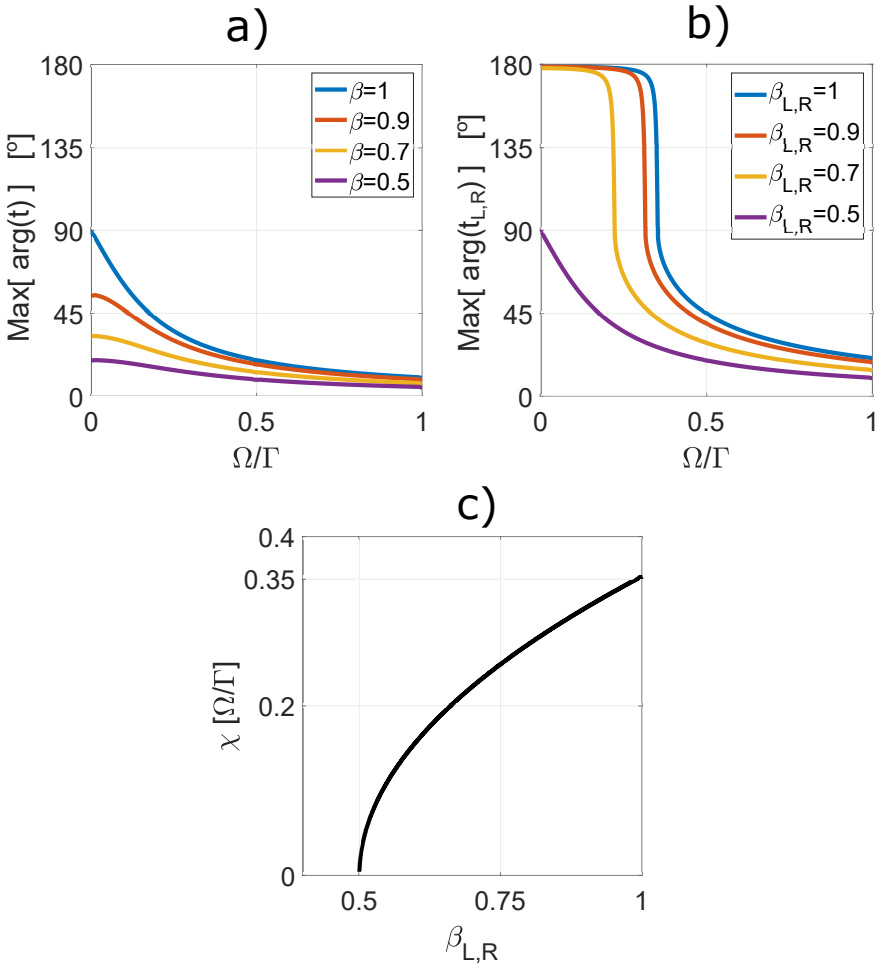

Figure 3.6: The maximum phase shift power dependence for a range of coupling factors (legends) for the isotropic a) and chiral case b). At Γ_{deph}. c) The sharp phase shift change point χ as function of $\beta_{L,R}$

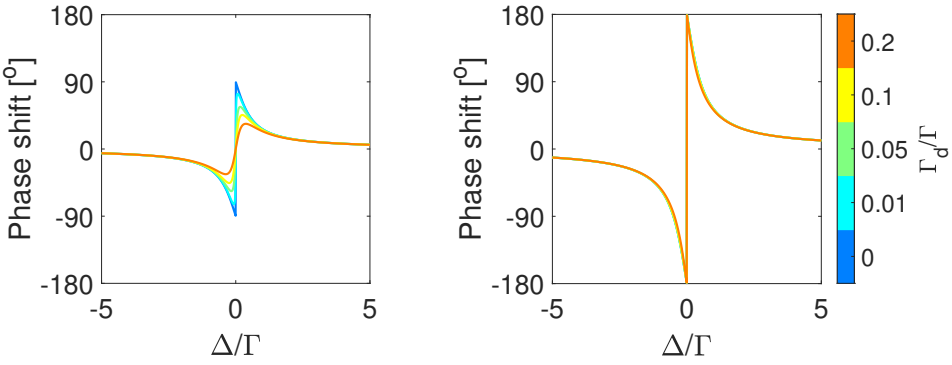

Figure 3.7: The spectral response of the phase shift for different pure dephasing rates, as indicated on the colorbar. For the isotropic (*left*) and the chiral (*right*) case.

The story seems here to be quite different between the coupling cases. Where the isotropic quickly gets a lower maximum achieveable phaseshift, the chiral stays undifferent. Here we have evaluated the phase shift up to $\Gamma_{deph} = 20\%\Gamma$ which is alot, when comparing to measured values of dephasing in litterature

3.3.5 The instantaneous phase shift switch in chiral coupling

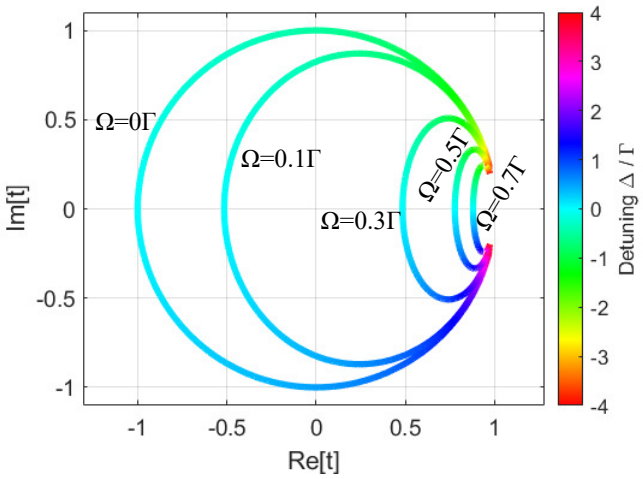

Figure 3.8: Complex space plot of $t_{L,R}$ as function of detuning(*colorbar*) for range of Rabi frequencies at $\Gamma_{deph} = 0$

Due to the transmission coefficient being a complex number it might be interesting to plot it in the complex space. In Fig. 3.8 the chiral transmission coeffiecient $t_{L,R}$ is plotted in the complex space as a function of detuning for different Rabi frequencies. It is here visible that $t_{L,R}$ draws out a circle in the complex space for low power and collapses that collapses to smaller ellipses for increasing power. Using this visualization one can directly interpolate the behavior of the transmission coefficient for a certain detuning as power is increased.

When evaluating the transmission coefficient at zero detuning the transmission coefficient purely takes on real values. When considering this for increasing power we can see that the transmission coefficient must cross origo in the complex plane coordinate system. This must ultimately mean that the phase shift will experience an instantaneous switch from 180^o to 0^o. To visualize it more literally we plot in Fig.3.9 the decomposed complex value of the complex transmission coefficient at zero detuning for a range of powers.

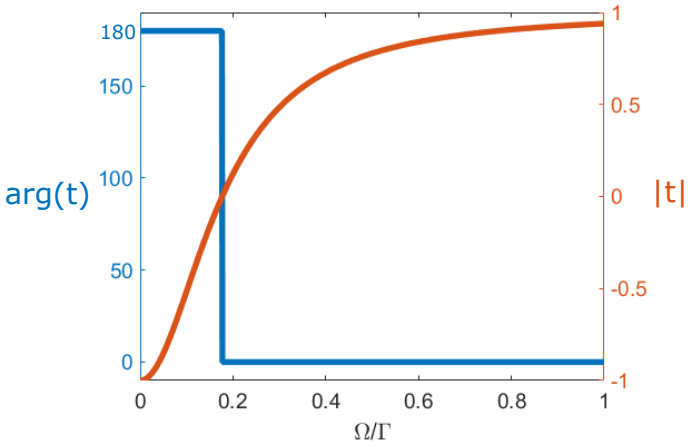

Figure 3.9: The phase(blue) and modulus(orange) of the complex transmission coefficient as function of power.

Here we observe that when the modulus $|t| = 0$ the phase shift experiences an instantaneous switch from 180^o to 0^o.

For this to be measurable we need a non zero intensity of the transmitted light. We saw earlier in Fig. 3.3 that at perfect coupling the chiral case yields unit transmission. We shall therefore try and compare the transmission intensity for several cases coupling strength to give an indication whether this phase shift is observable. In Fig. 3.10 we compare the transmission intensity to $t_{L,R}$ at zero detuning for a range a of $\beta_{L,R}$ factors and for a realistic $\Gamma_{deph} = 0.05\Gamma$, in order to see if the instantaneous phase shift is measureable.

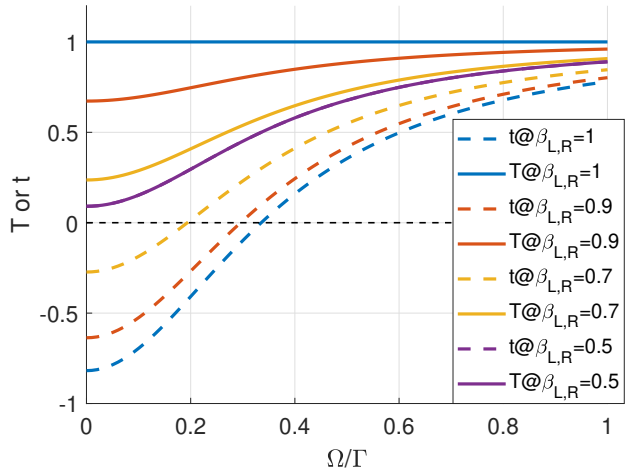

Figure 3.10: Transmission intensity(full line) compared their respective transmission coefficient (dashed lines)at different $\beta_{L,R}$ factors as indicated in the legends. For $\Gamma_{deph} = 5\%\Gamma$

We observe here multiple cases for $\beta_{L,R} > 0.5$ where the coefficient t crosses the zero line, thus indicating the phase shift switch from 180^0 to 0^o. While this is true the transmission intensity is still larger than 0. Ultimately indicating that this phase shift switch behavior would be possible to observe for chiral systems.

3.3.6 Realistic case for a PCW

In the real world setting in the lab we typically measure on QD in PCW waveguide with coupling to the range $\beta > 0.9$ and with dephasing in the range $\Gamma_{deph} = [0; 0.1]\Gamma$. In reference [21] they find $\beta > 0.87$ and $\Gamma_{deph} = [0; 0.12]\Gamma$ for a QD in a PCW. Conisdering these values we obtain the transmission intentsity and phase shift for low power as shown in Fig. 3.11.

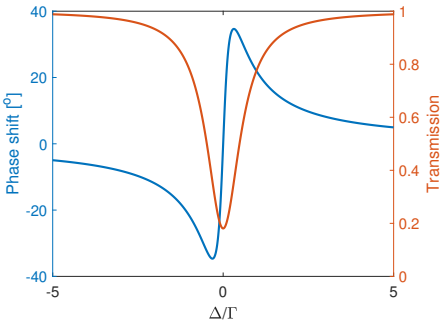

Figure 3.11: The spectral response for the phase shift and transmission, for $\beta = 0.87$ and $\Gamma_{deph} = 0.1\Gamma$

From this theoretical prediction we expect to have a maximum measureable phase shift of around 35^o with a on resonance transmission extinction at around 0.9. In accordance to this we should experimentally be able resolve such a phase shift.

Chapter 4

Experimental setup

4.1 Using a Mach-Zender interferometer to measure phase shift

The phase shift induced on the transmitted light is measured using a Mach-Zehnder type interferometer. The Mach-Zehnder interfeormeter consist intially of a BS that splits the input light into to different paths. After propagation the two paths is overlapped at a final beam splitter, as shown in the schematic on Fig.4.1. The output light from this beamsplitter then shows the interference signal. The intensity of this signal depends of the phase difference between the light obtained in one path compared to the other. The phase shift arise from either the path length difference, experimental equipment or interaction with the quantum dot. The intensity of the output is measured by photo detectors, call them here A and B. The normalized intensity on the outputs follow the relations below:

$$I_A = \sin((\varphi_E + \varphi_{QD})/2)^2 \qquad I_B = 1 - I_A$$

The intensity depends on the total phase difference $\varphi_E + \varphi_{QD}$ between the two paths. φ_E relates to that induced by the environment and the path length difference. φ_{QD} is the phase shift induce by interaction with the quantum dot. As explored in theory φ_{QD} were calculated from the complex transmission coefficient as $\varphi_{QD} = \arg(t)$. Thus it depends on detuning between the QD resonance and light field. This phase is then measured from the interference signal on one of the outputs, while scanning the light across resonance of the QD. However, output signal will also depend on the environmental phaseshift φ_E. To distinguish between the two, it is used that the QD resonance can be tuned electrically using the stark effect. Using this, φ_{QD} is then extracted as the difference between two subsequent measurements: One where the QD is tuned far off resonance and one where it is fixed to a certain frequency

close to resonance of the light.

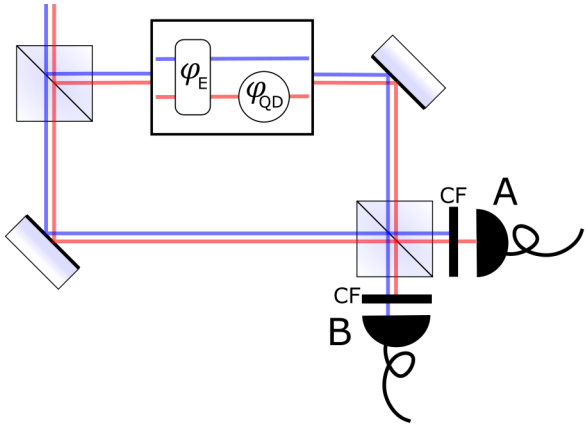

Figure 4.1: Principle of the Mach-Zehnder interferometer with a relative phase φ_E and φ_{QD} for QD resonant light. Detector A and B on the interferometer is filtered frequency wise by frequency filters (CF).

An experiment with the same methodology have been conducted where light interacting on a single trapped Rb^{87} ion [1]. A maximum phase shift of 1^o is observed.

The environmental induced phase shift is a source of large fluctuations in interferometeric signal. The main source of fluctuations comes path length fluctuations larger than than the wavelength of the light. These fluctuations has root in the vibration of the optical equipment. This were especially present since, the interferometer had an optical path length of approximately 3m, and were mounted on top of a cryostat with no measure of vibration dampening. Thus the interferometer had to be stabilized over the cause of a measurement. The stabilization is realized through mounting one of the interferometer mirrors on a piezo electric transducer(PZT), which enable linear displacement of the mirror and thus to change the path length difference. Fluctuations in the path length were thereby stabilized actively in a feedback loop that stabilize the output signal of the interferometer. However, if the stabilization were to be done on the light interacting with the quantum dot, the sought for phase obtained from to the interaction, would simply be compensated in the stabilization loop and the phase shift would not be measurable. To circumvent this, a second far off-resonant laser for stabilization is sent through the interferometer. The two colors are depicted on Fig. 4.1 with their respective obtained phase. By filtering the two colors at the outputs, they respectively be used for stabilizing of the interferometer and measurement of the quantum dot induced phase shift.

4.2 Experiment control and optical setup

Here we shall consider the optical setup used for experiment in the lab and later how the the surrounding equipment were controlled and used.

4.2.1 Optical setup

The setup consist of 3 free space optical setups connected by fiber. They will be presented as follows. 1) The Mach-Zehnder interferometer setup for measuring the phase shift. 2) Laser overlapping setup for introducing two different wavelengths in the interferometer. 3) A color filter setup using a grating to filter strong stabilization before a single photon detector.

1) Interferometer

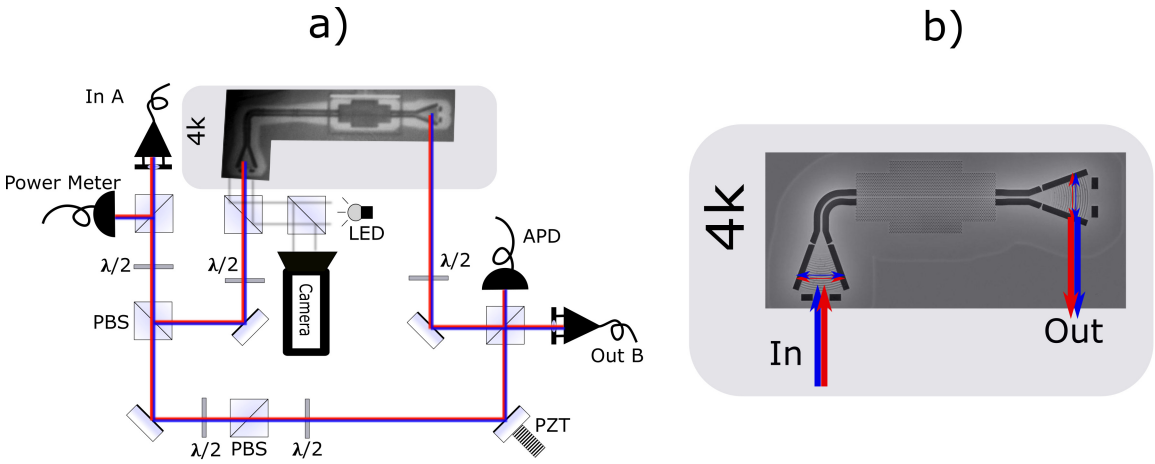

Figure 4.2: a) Optical setup of the interferometer. b) SEM picture of an example PCW

At the input (In A) of the overlapped laser light, a beam splitter redirect a part of the input to a power meter, for stabilization of the power in a feedback loop with *PID 2* as shown later on Fig. 4.4. Here both laser inputs is directed to the power meter, however stabilization laser has much higher intensity, such the power from the measurement laser can be neglected. Then a polarizing beam splitter (PBS) is placed the first beam "splitting" of the interferometer. Before this PBS, a half waveplate ($\lambda/2$) is used to adjust the polarization, and thus able to control the intensity of the light being led into both interferometer arms. The intensity would have to be controlled since the loss might be unequal in the two interferometer arms. Therefore, it is adjustable for setting the intensity equal at the interference in the

end.

The reflected beam is sent to the sample containing the PCW with an embedded quantum dot and the other is reflected of the PZT mounted mirror. The sample with the PCW is positioned in a cryostat and is cooled to 4K, in a low pressured (mbar) helium atmosphere. The sample is mounted on a PZT positioning stage at the end of an approximately 1 meter long cage, directly below the interferometer. In order to guide the light to the sample, in reality a beamsplitter would rotate the optical propagation from horizontal to vertical. Above the sample a microscope objective is used to focus and thereby couple light into the Input output gratings of the PCW, as seen on Fig.4.2.b). To match the optimal input polarization of the grating a $\lambda/2$ waveplate is installed. As indicated by the arrows on the gratings in Fig.4.2.b). In a similar manner the light from the output grating is also collected and collimated back into the interferometer arm using the microscope objective. Before interfering the two paths at the 50:50 beamsplitter, a $\lambda/2$ wave plate is installed to match the polarization, for maximum fringe visibility. Since the light loss is greater for the PCW transmitted path an additional power control is added on the PZT reflected path, using an additional $\lambda/2$ filter and a PBS .

Finally the two path is interfered on 50:50 beamsplitter. The outputs of the interferometer respectively have an avalanche photo detector(APD) and fiber coupling output(OUT B) installed. The APD is used to record the interference signal for the stabilization feedback loop. Both overlapped colors is measured on the APD, but due to the high intensity of stabilization laser light the other can be neglected. The fiber output is lead through a grating filter setup for filtering of the strong stabilization light, thereby allowing single photon measurement of the quantum dot interacting light.

Finally, in addition to the interferometer setup, a small camera is also installed to image of the sample. Here a beam splitter is positioned such that the light from a light emitting diode (LED) is directed towards the sample, and the camera can image the LED light reflection from the sample. This produces an image of the PCW as shown in the grey marked area on Fig.4.2.a).

2) Color overlap

Before the interferometer a free space optical setup were build to overlap the light from two lasers. The overlapping setup consist of two laser inputs of different wavelength that is overlapped into the same spatial mode and coupled into the same

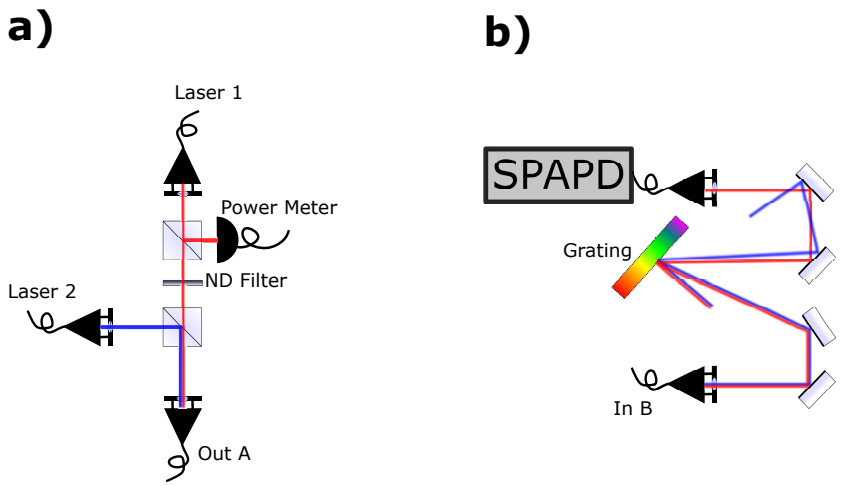

Figure 4.3: a) The laser overlapping setup. b) The grating filter before acquisition at the SPAPD

fiber. See Fig. 4.3.a). The QD resonant laser input (*laser 1*) is first partially reflected with a beamsplitter onto a power meter. The measured power is used for power stabilization, using *pid 1* as later shown on Fig. 4.4. Afterwards this light is spatially overlapped with off-resonant quantum dot laser light (*Laser 2*), and coupled into a fiber. This fiber is then routed to the interferometer setup.

3) Filtering of the strong stabilization light

The grating filter start by an input fiber (In B) that contains the interference signal from the interferometer output (Out B). This signal is then split according to its frequency into different spatial modes by using a diffraction grating. To filter away the stabilization light, a fiber output coupler is then aligned to the QD resonant (laser 1). This enabled the measurement of the QD resonant light without the strong stabilization light. This output is then measured using a single photon avalanche photon detector (SPAPD), that enables for the measurement of photons. The SPAPD is connected to a FPGA which count the number of events within a certain integration time. Hereafter, the integrated counts is sent by serial communication to be saved on the computer. the grating filter were measured to have transmission range of roughly 0.5nm around peak transmission. Thus the wavelength of the stabilization laser 2 had to be chosen outside of this range. Initially band pass filters were used. However they were found inadequate for filtering, as the photon measurement were completely drowned in light from the stabilization laser.

Along with the optics, the setup consist of many sub elements, that is controllable through a serial connection to a computer.

4.2.2 Experiment control

Fig. 4.4 show a detailed overview schematic of the entire experimental setup and the connection between sub elements. Here everything from the initial control of the laser sources to the end measurements were controlled and logged by communication to a computer.

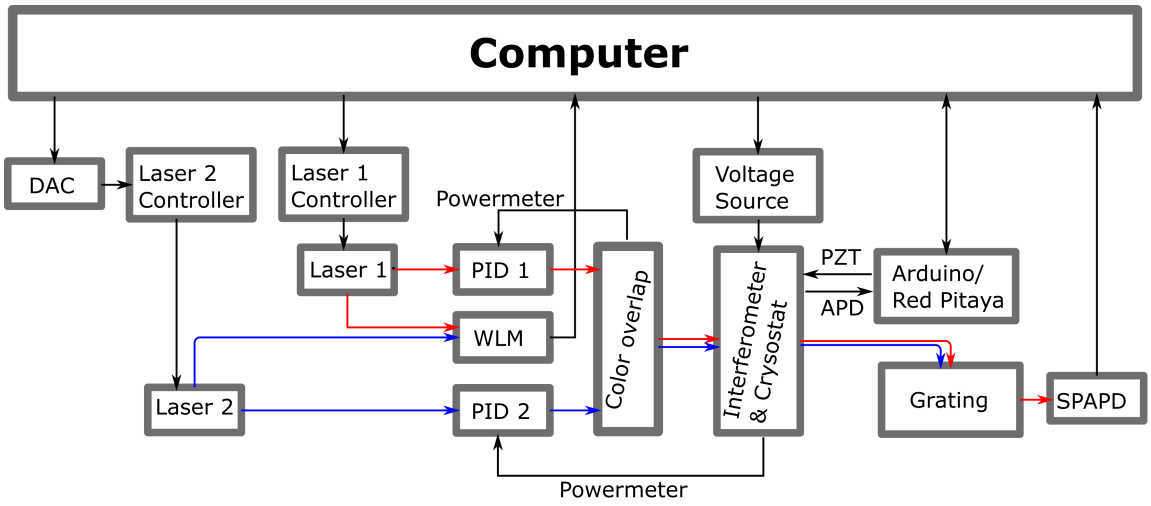

Figure 4.4: A layout of the interconnections between devices used in the setup. Black arrows indicate electrical connections and colored (Blue/Red) indicate laser lines for Laser 1 and Laser 2.

The schematic is drawn in a chronological ordered manner from left to right, corresponding to the experimental procedure. First the two lasers are initialized. Here *laser 2* is set off-resonant to the QD transition and is used for stabilization. *Laser 1* is used for measuring the of the phase shift. First, the laser wavelengths are stabilized to a specified wavelength, using a feedback loop with a wave meter (*WLM*). Laser 2 wavelength had to stabilized through an intermediate digital to analog current(*DAC*) device between the computer and laser controller.
Then the light output from the two lasers are connected with fibers into two separate power controlling-and stabilizing voltage controlled attenuators, controlled with PID loop(*PID 1,2*). The powers are stabilized to the power measured on two power meters. The are located in different free space optical setup, respectively the *Laser overlap* and *Interferometer*. After power stabilization, the two separate lasers are overlapped and combined into one fiber in the *Laser overlapping* setup. This fiber

routes the overlapped laser light to the cryostat and interferometer setup.
In the Mach-Zehnder interferometer setup, one path is coupled through a photonic wave guide with an embedded quantum dot. The resonance of the quantum dot can be controlled by the Stark effect via the *voltage source* that applies a voltage across the the sample diode.

After transmission through the wave guide, the light is overlapped back with the refference beam, using a mirror mounted on a *PZT*, used in the interference signal can be stabilized on an avalanche photo detector by a feed back loop. The feed back loop response is controlled using an *Arduino Due* microcontroller or a *Red Pitaya* (See next section).
The other output of the interferometer that is not used for, the stabilization feedback loop, is sent through a wavelength filtering grating system. This enables the filtering of the strong stabilization light from laser 2. This allows the measurement of single photons experiencing a phase induced by the QD on a single photon APD (*SPAPD*).

Controlling the setup like this, enables the the measurement of data and change of many device parameters on a short time scale.

4.3 Stabilization of the interferometer

Mechanical fluctuations on the order of the laser wavelength will be imprinted as huge fluctuations on the interferometer output signal. As previously described one of the mirrors in the interferometer arm is mounted on a PZT. By applying a voltage across the PZT it will expand and linearly displace the mirror. Thereby allowing to adjust the path length of the interferometer arm for compensation of the fluctuations. The PZT used in this case have a range of $5\mu m/1000$V. In order to stabilize the interferometer, this voltage is controlled by a feedback loop with the interferometer output.

Initially an Arduino[3] was used to stabilize the interferometer using an home written algorithm inspired by reference [17]. This method was later replaced by the use of Red Pitaya[39] with a processor and field programmable gate array (FPGA) was used to implement a lock-in amplifier and PID loop. A closer look on these methods will be taken in the following sections.

4.3.1 Stabilization with a Arduino micro controller

Arduino provides a range of different micro controllers. The micro controllers supplies a controllable interface between a series of inputs and outputs. The one used here is the Arduino Due, because of its digital to analog current(DAC) output. The voltage produced by the APD mesuring the stabilization light output is measured by the Arduino's analog to digital (ADC) input. Initially to test the response, a ADC voltage output was used to control the PZT while the corresponding interferometric signal was recorded on the DAC input. In Fig. 4.5 shows the result of sweep of the fringes by modulating the ADC voltage with triangular signal.

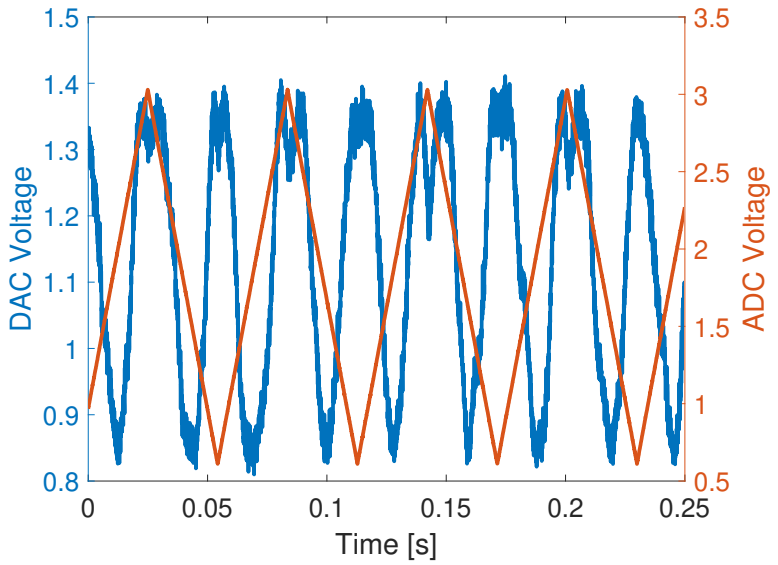

Figure 4.5:

Here we observe that the interferometer response is just a bit more than a period for each modulation. Meaning that we in this case is able to resolve an entire fringe period of the interferometer. The ability to interfere can be defined by interferometric visibility v defined as:

$$v = \frac{f_{max} - f_{min}}{f_{max} + f_{min} - 2B}$$

Where f_{max} and f_{min} is the maximum and minimum fringe value and B is the background signal. The result sweep in Fig.4.5 corresponds to a visibility $v \sim 0.2349$. Obtaining a high visibility is experimentally hard as the interferometer consist of many optical elements and hos to be reflected directly of the GaAs sample. This

alternates the light mode and ultimately the visibility of the interference.

Knowing that the interferometer can be controlled with the PZT a program can then be written for stabilization, by controlling the DAC output depending on the ADC input, on the idea from reference [17]. The general working of the program, is to keep increasing or decreasing the DAC voltage such that a newly measured ADC value from the APD is higher than the last, and if not then the direction of change in the DAC voltage is reassigned. This will stabilize the interferometer at a maximum output intensity output on the APD. Around which it will make some small oscillations.

In this project the the stabilization method slightly is expanded, for the stabilization at any output intensity i.e. phase. Instead of searching for maximum intensity on the output, the same algorithm principle is used to minimize an error between the currently measured output and wanted output. The error is defined as the difference between a goal value defined on the entire output fringe range and a currently measured value (y). These point is also defined in Fig, 4.6, that visualize one fringe period.

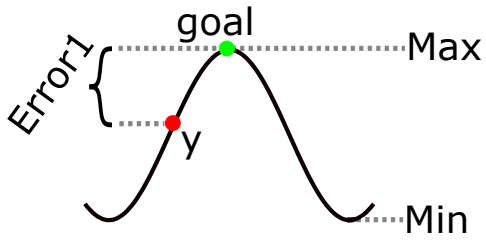

Figure 4.6: An interferometric fringe labeled with Min and Max used to define the fringe range, and Error1 defined as the difference between y and goal.

In order to set a goal value on the fringe range it first has to be mapped. To map the fringe output range, a scan is performed by sweeping the PZT with a triangle signal that displaces the PZT by more than a wavelength of the interference light. Therefrom the minimum(Min) and maximum(Max) ADC values of the can be collected to infer the fringe range of the interferometer. From this range, the wanted goal can be defined, and allow the interferometer to be stabilized at any phase defined in the fringe range. However, as the focus here was to do a first measurement of the phase shift, the stabilization goal is kept constant at maximum of the interferometer signal, for measurements presented here.

The entire program running on the Arduino it consist of a loop of two major algorithms, as shown on the flowchart in Fig.4.7. For every 1 in 10000 loop iteration,

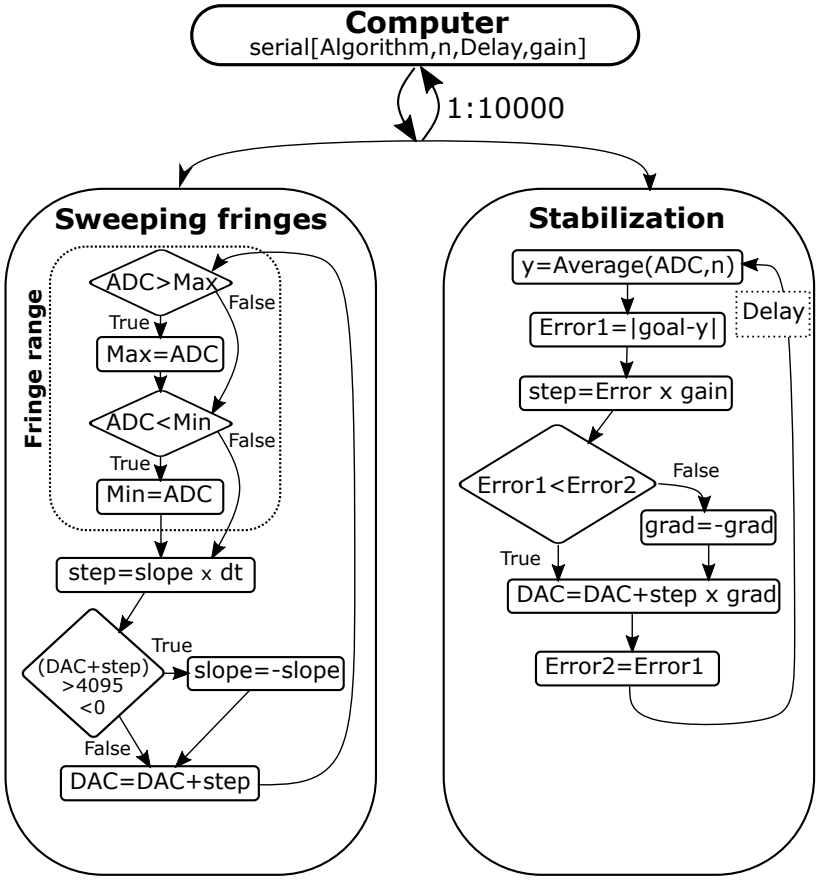

Figure 4.7: Flowchart of the program running on the Arduino. Top block indicates computer serial communication for 1 in 10000 program iteration. *left*: Flowchart of the fringe sweeping algorithm. *right*: Flowchart of the stabilization algorithm.

the Arduino reads a serial message from the computer. The message contains four variables. The variable *"Algorithm"* decide which algorithm to be run ie. *sweeping of the fringe range* or interferometer *stabilization*. The rest three variables *n,Delay,gain* are used in the interferometer stabilization algorithm. The algorithms are described as follows

- **Sweeping of the fringe range:** The DAC output of the Arduino is driven in its entire digital 12bit (0 to 4095) to produce the sweeping signal. When it reaches either the bound 0 or 4095, the step gradient change sign. The DAC step is calculated by $step = dt \cdot slope$. Where the slope is predefined for a certain modulation frequency and dt is the time difference since last iteration. For each iteration the maximum and minimum ADC value is logged and saved

to variables *Max* and *Min* respectively, if its bigger or smaller than previous values (Dashed line box), thereby retrieving the fringe range, to set the stabilization goal.

- **Stabilization:** Initially an average input value y from the APD is calculated for n subsequent measurements of the ADC. Then the current error value *Error1* is calculated as the difference between y and the *goal*. With *Error1* the next *step* value to be added to the DAC value is calculated as $step = Error1 \cdot gain$. The direction of the step is then decided: if current*Error1* is bigger than the old error *Error2* from the previous iteration, then the step direction is reversed by changing sign on the gradient parameter *grad*, which can take the values 1 or -1. At last, the current *Error1* is redefined to *Error2* for comparison in the next loop iteration. Before looping back a *Delay* in units of microseconds is added to before starting over. The Delay is introduced to avoid over driving of the system, which would destabilize the interferometer, as the PZT response time is slower than the update rate of the Arduino output.

An example of the application of these algorithms are showed in Fig. 4.8

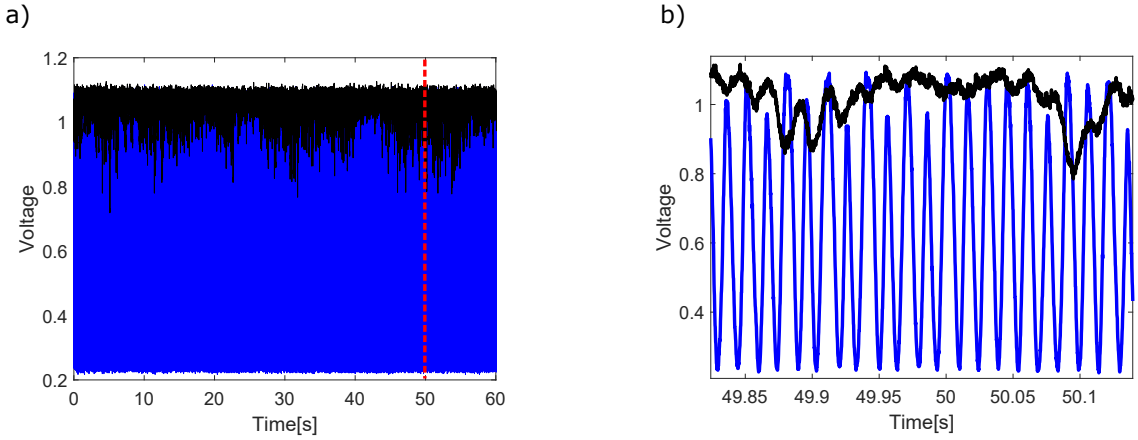

Figure 4.8: Example of the stabilization (*black*) overlapped to the corresponding sweep of the fringes(*blue*). a) shows for 60 second acquisition. b) A zoom corresponding to the data on dashed red line in a).

It is evident that the staiblization signal is mostly located at the top of the fringe, and thus seem to work. Since we are at a maximum of the fringe function it is not possible to apply the central limit theorem method for estimating the phase uncertainty of the stabilization. However we can define a figure of merit that estimates the fluctuation of the stabilization phase to maximum fringe phase ie.π. By fitting a straight line to the lower and upper 5% points of the entire fringe range, the

entire fringe range R_{fringe} can be inferred. Using this range along with the standard deviation of the stabilization signal σ_{stab}. we can write the phase fluctuation δf as:

$$\delta f = \pi - 2 * \sin^{-1}\left(\sqrt{1 - \sigma_{stab}/R_{fringe}}\right) \tag{4.1}$$

Applying this method method to the data displayed in Fig. 4.8,a phase fluctuation of $\delta f = 25.4^o$ is obtained.

By being able to changing the stabilization parameter with the serial message we can adjust the parameter values for best stabilization. In Fig. 4.9 The phase fluctuations is displayed for a sweep of the *delay* and *gain* parameters.

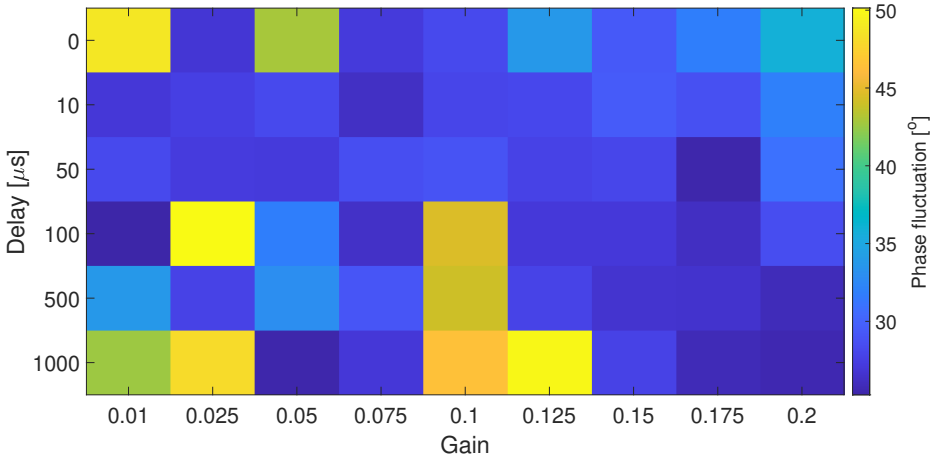

Figure 4.9: Phase fluctuation scale on the colorbar for n=50 the delay time and gain is swept.

Though the results seem to be really diverse, there seem to be some slight trend of lowest phase fluctuation along the diagonal, from low gain and short delay to high gain and long delay. This makes sense as longer delay times leads to bigger drift and thus need higher gain to compensate. The best area seems to at both high gain and delay time.

While Fig.4.9 doesn't cover the entire parameter space, it was observed experimentally that setting the gain higher wouldn't decrease phase fluctuation indefinitely.

A similar scan presented in Appendix A.1, was done in the 3D parameter space that included the averaging number n as well. This measurement indicated that in general a averaging number below 100 showed less fluctuations at a wider range of

delay times.

Jumps in the fluctuations, to adjacent parameter points can be present for both measurements. Since large temporary and occasional fluctuations were observed. These fluctuation were induced due to fluctuations in the power or wavelength of the laser. They could also arise on smaller time scales, if somebody were to mechanically disturb the interferometer. Nonetheless, we could infer from general tendencies, a good set of that parameters for interferometer stabilization.

4.3.2 Minimizing mechanical induced fluctuations

Initially a smaller interferometer was build on an optical table, to test the stabilization . The interferometer used in the final experiment, were constructed directly on a breadboard(smaller metal plate for mounting optics on) mounted directly on to the casing of the cryostat by six metal rods. This installation introduced much more noise on the interferometer than while installed on the optical table, which is dampened for mechanical vibrations and fluctuations. Fig. 4.10 show an initial test of the stabilized compared to a non-stabilized interferometer, on both the optical table and cryostat.

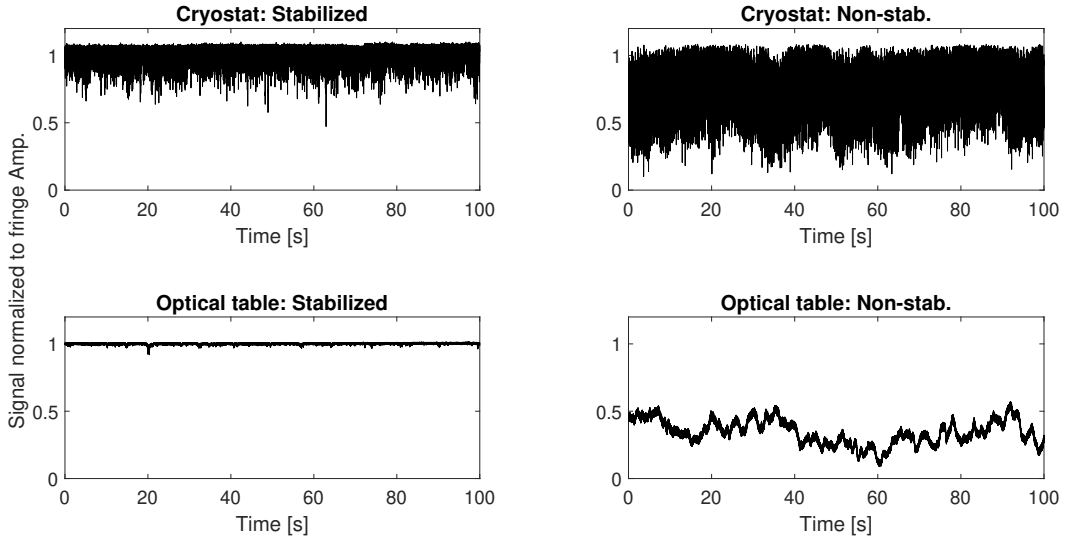

Figure 4.10: Comparison between the initial test between stabilization of an interferometer on the optical table(*top row*) and stabilization on the cryostat (*bottom row*)

the challenge of compensating for these fluctuation can directly be seen the Non-stabilized signal from the cryostat breadboard to the optical table. Non-stabilized cases is of a higher fluctuation amplitude and frequency, for the cryostat compared to the optical table. This of course translates directly to fluctuations when stabilizing the interferometers. Calculating the phase fluctuation of the stabilization, yields $\delta f_{table} = 8.2^o$ and $\delta f_{cryo} = 23.9^o$, respectively for the optical table and cryostat installed interferometer. For further investigation, the data in Fig.4.10 is considered in frequency space in Fig. Fig.4.11.

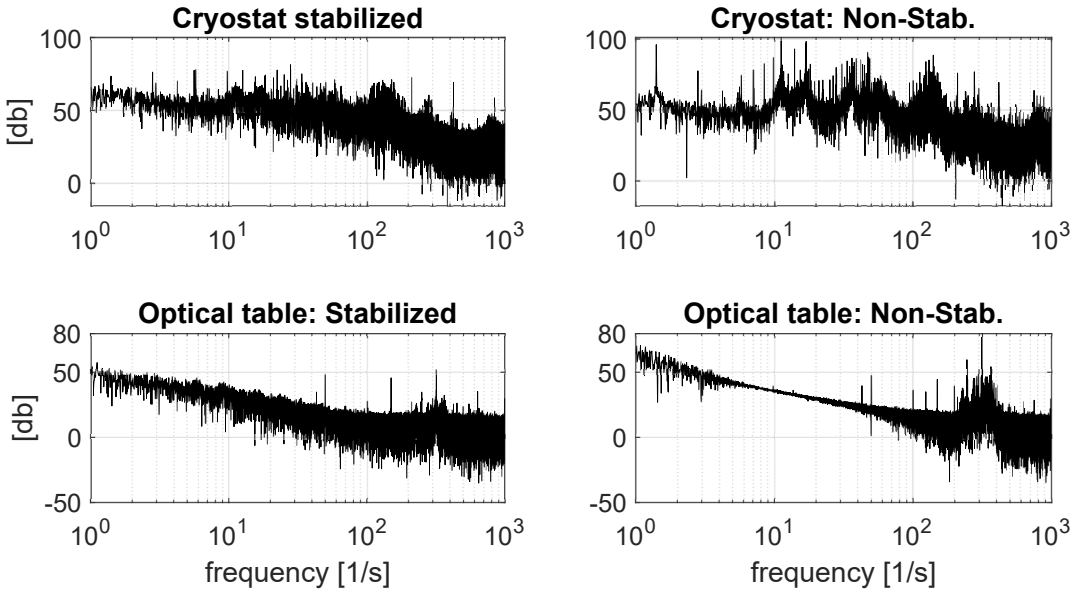

Figure 4.11: Comparison between the initial test between stabilization of an interferometer on the optical table(*top row*) and stabilization on the cryostat (*bottom row*)

From this it is again clear that the interferometer mounted on the optical table is subject to much less prominent fluctuations in most of the spectrum. From the comparing the fluctuation spectrum between the stabilized and non-stabilized, can see that the stabilization dampens the fluctuations spikes that are visible throughout the non-stabilized spectrum, Indicating we are able to stabilize fluctuations up to a 1000 Hz. However, only on bigger and prominent fluctuations. This can be seen on the spectrum for the optical table data. Here we observe in the non stabilized case a smooth linear range is highly affected when the stabilization is applied.

In an attempt to reduce the mechanical noise, rubber spacers were installed in between the metal poles and the breadboard. This were done in the beliefe that the cryostat casing which is much bigger than the optical equipment, would induce mechanical noise collected from the environment as well as shaky compressor lines connected to the cryostat. Afterwards a prominent noise on around 50 Hz was introduced on the output signal of the interferometer. Initially one would think that this would correspond to electrical noise from the 50 Hz noise from power supplies of the equipment. However, it turned out to be a resonance frequency of breadboard combined with the optics. Instead of allowing this noise to be drained through the cryostat casing, the rubber had isolated breadboard and optics system. Results regarding this has been supplied in appendix A.2.1. The noise induced by the compressor was seen to be small, when comparing the noise spectrum for when the compressor was on to when it was switched off, see appendix A.2.2.

Other than mechanical fluctuation noise, a big source of noise is from the electric noise on the APD. The APD introduces quite high electric noise comparable to the mechanical fluctuations, due to the fact that the intensity of the transmitted light through the wave guide is highly attenuated, and thus the internal gain of the APD has to be increased. Increasing the APD gain furthermore increases the electric noise on the output signal. A measurement of the background signal noise induced by APD indicated that it correspond to a fake phase fluctuation of $\delta f_{APD} = 13.4^o$. of the case shown in Fig. 4.10.

Power fluctuations of the laser light will also directly influence the amplitude of the fringes on the interferometer output. This will render previously set stabilizaton goal from the fringe sweeping, to be false according to the stabilization wanted. Therefore the power has to be stable throughout the measurement. For longer measurements the fringe might have to be swept repeatedly to reassure the correct stabilization.

4.3.3 Change of stabilization method

When preparing for the phase shift measurement. It turned out that even while the stabilization light is far off resonant to the to QD transition it still had an effect. This is displayed through a scan of the transmission across the QD resonance while also having the off-resonant stabilization light on. Fig. 4.12 shows a series of measurements of the transmission dip for a series of different powers for stabilization light.

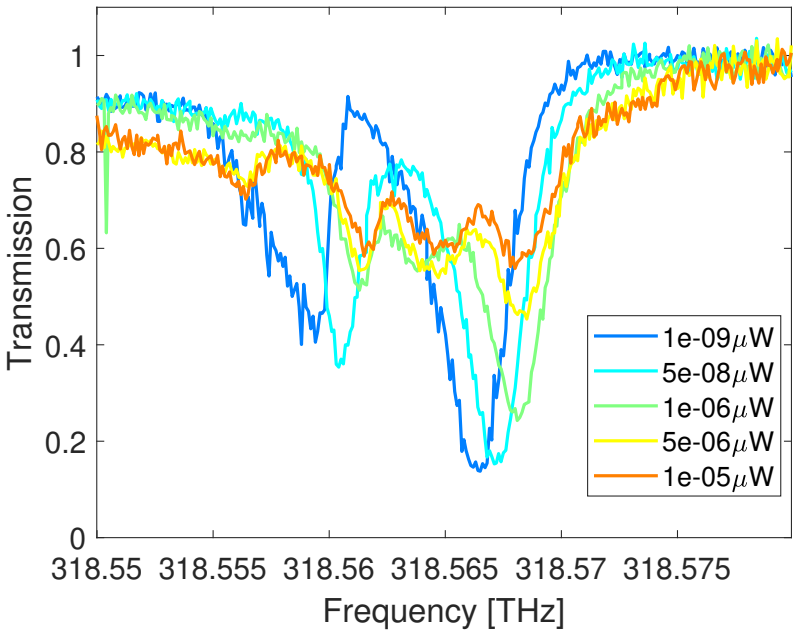

Figure 4.12: Normalized transmission spectre of resonant light while increasing power of the off-resonant stabilization light as indicated.

The data shows that the QD is affected while increasing the power of the stabilization light The transmission dip seems to decrease its amplitude while tuning the resonance to higher frequency. For Higher powers the most prominent dip seems to split into two. The underlying physics of this effect.

The stabilization, using the Arduino would need stabilization powers well into tens of μW in order for the APD output to cover enough of ADC range for stabilization. However, this power is enough to reduce the transmission dip significantly and introduce a second transition, as observed on Fig. 4.12.
Thus another method of stabilization, with the ability to stabilize at low power were needed.

Stabilization using an lock-in amplifier and PID loop

To realize stabilization at lower power, the commercially available Red Pitaya[39] as used. Red Pitaya supplies a programmable system with a 14 bit input/output at an working rate of 125M samples/s. Thereby enabling measurement of smaller output fluctuations at a higher rate than the Arduino Due. This system was first introduced late in the project when this tuning of the power became apparent.

For the stabilization with the Red Pitaya a combined lock-in amplifier along with a PID loop was used. Using an open source pre written program from reference [27]. This program allowed both the implementation of the lock-in amplifier and the PID loop using only the Red Pitaya.
By using a lock-in amplifier low amplitude signals can be extracted from the APD. Thereby allowing a low stabilization laser power. The output value from the lock-in Amplifier is then used as an error signal in a PID feed back loop. The lock-in amplifier error signal is proportional to the time derivative of the interferometer output, and by stabilizing to zero of the lock-in amplifier output the stabilization is effectively at the maximum or minimum of the interferometer fringe. Results are displayed in Fig. 4.13.

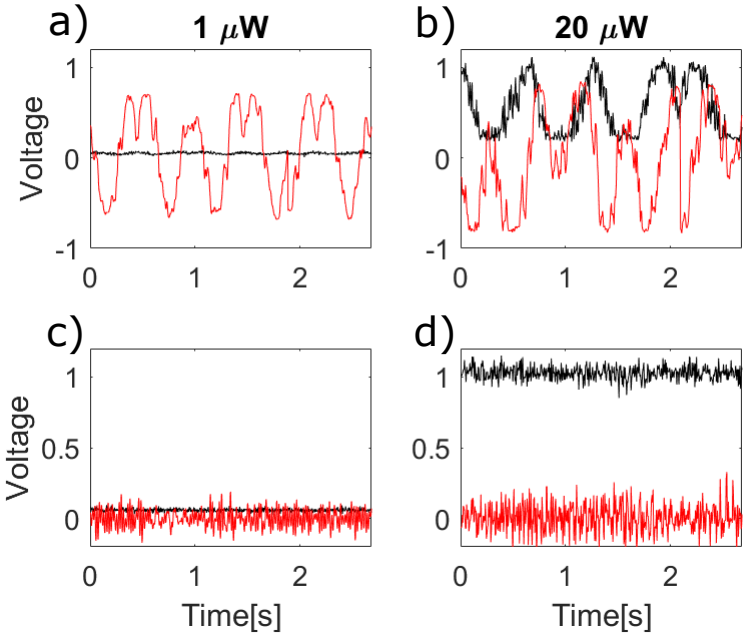

Figure 4.13: For all plots: Black is the input from the APD and red is the lock-in amplifier output. a) Sweeping of the fringes at $1\mu W$. b) Sweeping of the fringes at $20\mu W$. c) Stabilization at $1\mu W$. d) Stabilization at $20\mu W$.

The same pair of measurement were here performed for two powers, $1\mu W$ and $20\mu W$, of the stabilization laser. In order to resolve the signal measured from the APD, for qualitative analysis. We observe here for the fringe sweeping at $20\mu W$ (Fig.4.13.b) that the lock-in output indeed produce a signal proportional to the APD signal.This is seen to be reproducible even at the low power of $1\mu W$, where the lock-in amplifier still outputs a prominent signal, usable for stabilization. In

the situation of stabilization as shown in Fig.4.13. c) and d). The lock-in signal is well centered around 0, thus indicating the stabilization of the interferomter. To evaluate the method, a time trace of the PID stabilization at $20\mu W$ is compared-and normalized to the fringe range is shown in. Fig.4.14. This corresponds to a phase fluctuation of $\delta f = 28.1^o$

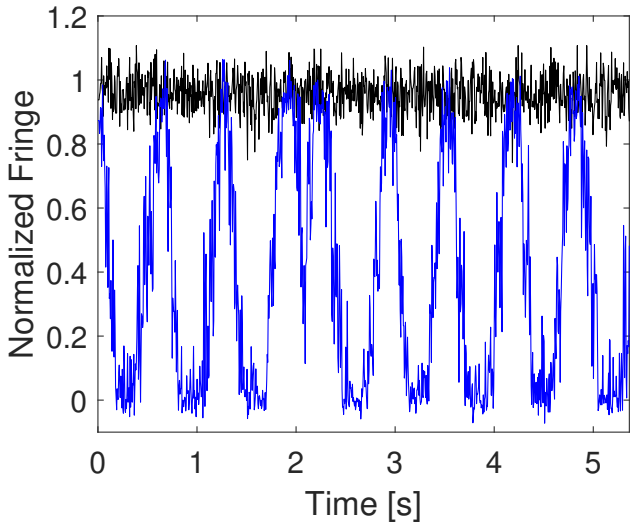

Figure 4.14: The Stabilization signal(black) normalized and overlapped to the fringe signal(blue) at 20 $/muW$ locking light

This result shows that introducing the lock-in amplifier and PID loop using the Red Pitaya enables stabilization of the interferometer with a phase fluctuation comparable to that realize with the arduino. In contrast to the Arduino method, this enables the stabilization at low power of the stabilization light. Thereby allowing stabilization without affecting the QD transition.

4.3.4 Improving stabilization with an amplifier

The best phase resolution per digital value in the Arduino or the Red Pitaya, is obtained when the fringe output from the APD covers the entire ADC dynamic range. Thereby increasing the sensitivity of phase fluctuations and eventually enabling a finer compensation to phase fluctuations.
The voltage output of the APD is proportional to the the power emitted on the sensor and the adjustable internal gain. In order to match the APD output to the dynamic range of the ADC input, increasing the power isn't a possibility as it would worsen the QD transition as seen in Fig. 4.12. Thereby only allowing the output

to be matched via the gain. However, increasing the gain will also increase a DC voltage, ultimately rendering the bottom of the ADC range useless, since both the Arduino and Red Pitaya ADC starts at 0 voltage. The dynamic range of the Red Pitaya is

The Arduino has dynamic range from 0V to 3V mapped over 12 bit ADC range, corresponding to a resolution of 4096. While the Red Pitaya input is between 0V to 1V mapped over an 14 bit ADC range, corresponding to 16384 values.

In order to match the ADC ranges to the APD output, an amplifier was designed for use in this specific case. The designed amplifier has the function of being able to substract an offset to the APD output such the minimum fringe intensity value would go towards zero and afterwards amplify to match the given dynamic range. The amplifier circuit as presented in Fig.4.15 is based on operational amplifiers(OP-amp).

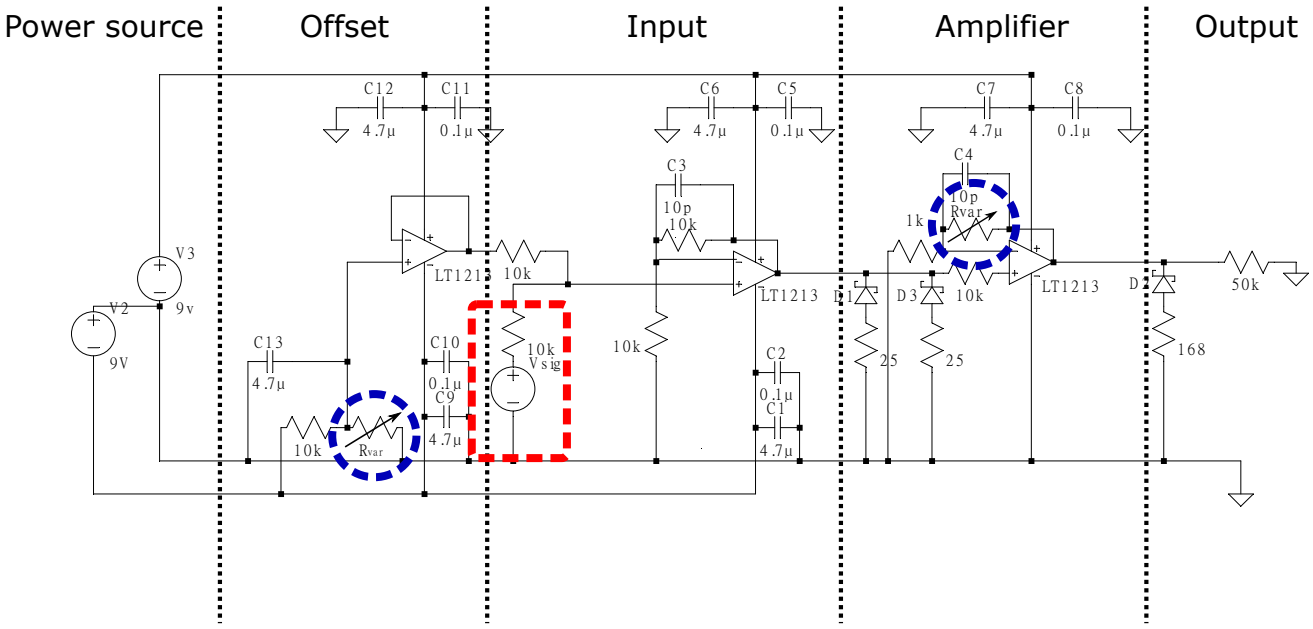

Figure 4.15: Circuit of the designes amplifier. Dashed lines divide the circuit into subsections as indicated by the headlines. The input signal is indicated by the red box. The adjustable potentiometers for the offset and gain are indicated by blue rings.

This circuit is build around 3 OP-amps, each with their respective function in different stages: Offset, Input and Amplifier as labeled on the schematic in Fig.4.15. In the offset an OP-amp is used to output a constant negative voltage. This negative voltage is later used to offset the input signal from the interferometer by a

summation operation. Then the signal is amplified before the output. The outputs is here simulated as the $50k\Omega$ resistor. Both the offset and the Amplification gain can be adjusted by the user via implemented potentiometers.

Initial test while building the amplifier (Fig.A.7.) showed to be able to reproduce the oscillatory signal without any significant phase delay up to 500KHz.
This circuit be used in future experiments to enhance the phase stabilization. And perhaps allow the re-implementation of the Arduino. A future implementation to the circuit could be to control the gain and offset in a feed bacnk loop, to allow the full mapping of the fringes on the ADC at all times

Using the ability to stabilize the interferometer while maintaining a QD transition, we now turn to the experimental effort at measuring the QD induced phase shift.

Chapter 5

Experimental realisation of the phase shift measurement

5.1 Overview of the system

5.1.1 Search for a highly coupled QD

To attempt the phase shift measurement, a QD transition in first have to be found. The QDs are fabricated using self-assembling methods. This result in the QDs being positioned in random positions throughout the sample[38], while also being randomly distributed in terms of resonance frequency around 930nm. Thus when fabricating the PCW onto the sample, the QD will also be randomly positioned in these. Since the QD coupling to the waveguide highly depends on the position of the QD within PCW, it alters the response of the QD equally random. Therefore, a big part of the experimental process is to first scan the structures to find a suitable QD. The method used here is to do a wide scan of the spectral response of the transmission through the PCW. After finding the general photonic response of the waveguide a scan of finer resolution is done across the bandedge spectrum. Specifically a QD close to the bandedge is of interest due to Purcell enhancement of the QD. This leads to a faster decay rate into waveguide modes comparable non-emitting decoherence ie. dephasing or transitions other QD resonant states [33]. Here measurements is done for a QD embedded in a PCW, which we in the theory of chapter 3 saw to give rise to a large extinction at good coupling and low dephasings. Therefore the QD can be recognized as highly extincting dip in the transmission. We search for a QD with a spectral width on the GHz scale. However this method would not be optimal for the chiral coupled case of a GPW, as the transmission will go towards unity for high coupling an low dephasing.

This procedure had to be repeated for a range of different waveguides before identifying a suitable QD. Here the results of the identification, for the quantum dot used in the final measurements is presented.

Transmission scan of the waveguide

The spectral scan of the transmission were simply done by blocking one path of the interferometer, and record the light being transmitted through the waveguide. The laser 2 used for the stabilization is turned off during this measurement. The transmission scan for the PCW used here is displayed in Fig. 5.1.

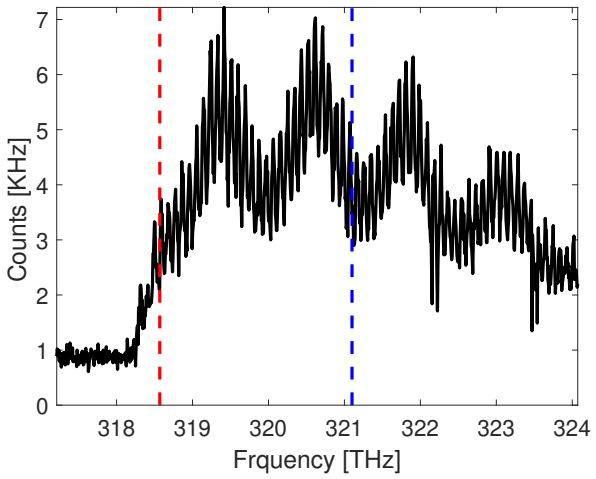

Figure 5.1: Transmission(*black*) measured as photon counts in KHz. *Red* dashed line shows QD resonance and *blue* is the frequency of the stabilization laser.

We can observe a range below approximately 318.3 THz where the data show a constant and low rate. This area corresponds to the photonic bandgap of the PCW, that allow no propagating waveguide modes. The 1 KHz counts corresponds mostly to stray light from the laboratory background. At higher frequencies the bandedge is visible as a quick rise in the transmitted counts. There is a variety of features in the transmission other than the bandgap. The most prominent is the regular oscillatory behavior. This is due to cavity-like features in the waveguide that reflect light. The reflection could arise from fabrication defects or transition areas, such as between grating inputs and waveguide. Multiple cavity behaviors must here be at work here, due to both slow and fast periods, as can be seen in Fig. 5.1.

High extinction of a QD in a waveguide

In order to locate a quantum dot spectrally, a similar scan at higher frequency resolution is done of the transmission across the bandedge. Here, a promising transmission extinction was found, as shown in Fig. 5.2. The QD resonance was found at around 318.66THz and is indicated by the red line in Fig. 5.1. It can be seen that it is indeed situated close to the bandedge. This dip has an extinction of around 80% at resonance and is the largest transmission extinction found during this project.

The frequency of stabilization laser 2 is well distanced from QD resonance, in an area of higher transmission, as indicated by the blue dashed line in Fig.5.1. This is chosen for increasing the signal for stabilization while maintaining low power as possible.

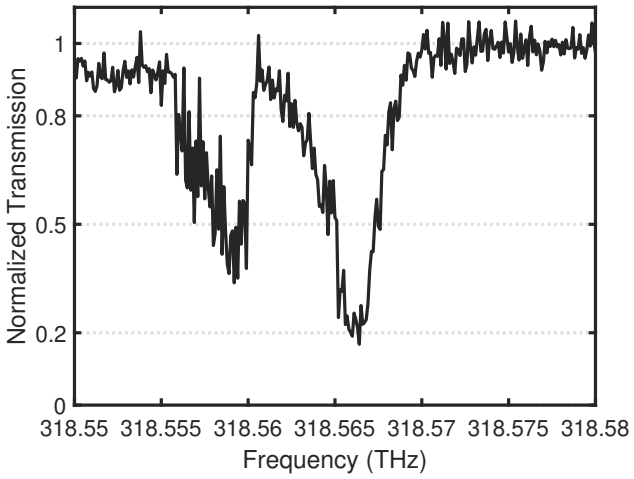

Figure 5.2: The transmission measurement normalized to background counts for the QD transition.

As also observed on Fig. 5.2 the QD showed an additional less extinctive transition at slightly lower frequency. This could be due to the fact that the light couple to two different dipoles of different polarization in the QD. In order to confirm that these transmission extinctions were indeed corresponding to a quantum dot, a scan is done to see the tuning of the QD resonance as function of the voltage applied across the diode (See chapter 3.). By tuning the voltage for a series of fixed frequencies we obtain the 2D results shown in Fig. 5.3. For more information, the data taken in Fig.5.2 was taken at a constant voltage of 1.24V.

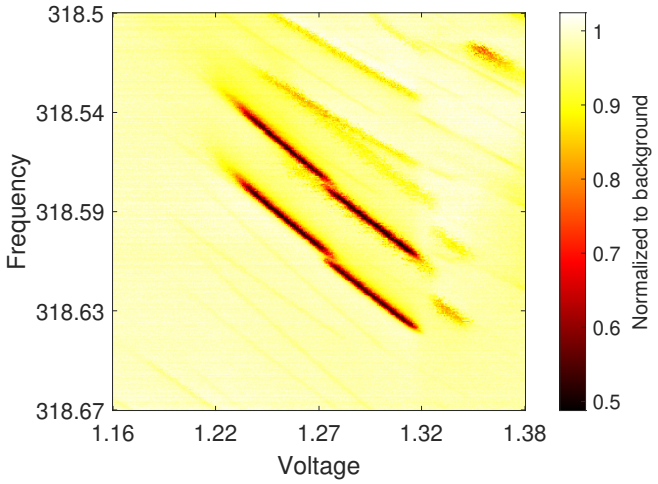

Figure 5.3: 2D intensity plot of the transmission normalized to maximum count rate for each voltage sweep.

This shows that the QD resonance indeed tune as a function of voltage. Thereby, showing its sensitivity to the Stark shift effect. Furthermore, both transmission extinctions seems to follow the same gradient of tuning, indicating that they indeed correspond to the same quantum dot. Using a peak-finding algorithm the resonance frequency of the large transmission extinction can be found at different voltages. By fitting a linear line to this, we find that the quantum dot tunes with a slope$of(0.72\pm$ 0.01)THz/V. This tuneable feature of the quantum dot will be used to tune the QD far away from resonance and to a fixed voltage corresponding to a frequency close to resonance with the light. Effectively turning the QD "on" and "off" for different measurements.

5.2 Measuring the phaseshift

With this QD candidate, we can now aim to measure the spectral response of the phase shift induced by the QD. To do this, the frequency of laser 1 is tuned across QD resonance while stabilizing the interferometer with laser 2. We know from theory that the transmission coefficient in Eq. 3.9 and 3.10 evolves as function of the detuning Δ. An thus the phase shift on the laser 1 light will also be subject to a detuning dependent phase shift. using the same denotations as in section 4.1 we can write:

$$\varphi_{QD}(\Delta) = \arg(\mathrm{t}(\Delta))$$

Furthermore, scanning the frequency of laser 1 gives rise to an additional frequency dependent phase due to the path length difference δL. We set this to be the envi-

ronmental dependent phase shift:

$$\varphi_E = \delta L \frac{2\pi}{\lambda}$$

This equation assumes freespace propagation, which of course is not true as the interferometer path consist of optical elements and the sample. However, we can use this equation to see that scanning laser 1 must give rise to an additional phase modulation in the interferometer output. This phase also gives rise to the phase fluctuations from mechanical noise, due to fluctuations altering the path length difference. It is here assumed that it is well stabilized.
To distinguish between the phase shift induced by the envirionment from the QD. We use the fact that the quantum dot can be turned "on" or "off" using the voltage tuning as in Fig. 5.3. The total phase obtained in the interferometer φ is then given by:

$$\varphi = \begin{cases} \varphi_E + \varphi_{QD} = \delta L \frac{2\pi}{\lambda} + \arg(\mathrm{t}(\Delta)) & \text{QD on} \\ \varphi_E = \delta L \frac{2\pi}{\lambda} & \text{QD off} \end{cases}$$

φ_{QD} can be found by measuring two subsequent measurements, one with the QD "on" and another with the QD "off". Taking the difference between these two measurements allows then to omit φ_E and retrieve φ_{QD}.
Scanning the frequency across resonance gives rise to the expected interferometer output shown in Fig. 5.4.

The interferometric curve is here plotted for a short path length of 15 cm for better visualization, and with $\beta = 0.9$. Corresponding to a maximum phaseshift of 56^0. We observe that the signal with the QD tuned on(blue), is offset compared to the environmental signal(orange) for the QD tuned off. From these two signals the phase shift can be found as the phase difference between the corresponding signal peak or valley of the fringe signal. Using this method the phase shift of the experimental results can be obtained.

5.2.1 Experimental results

A small part of the fringes experimentally measured is shown in Fig.5.5.a). The fact that we are indeed able to resolve the fringes is a testimony to the stabilization of the interferometer. The most obvious feature is the difference in the amplitude between the two measurements, which stems from the transmission intensity response to detuning. One has to look a bit more careful for observing the phaseshift directly, but it can be seen towards a detuning of 1 GHz. It is here visible that there is a slight offset between the signla when the QD is tuned on(blue) and off(organge).

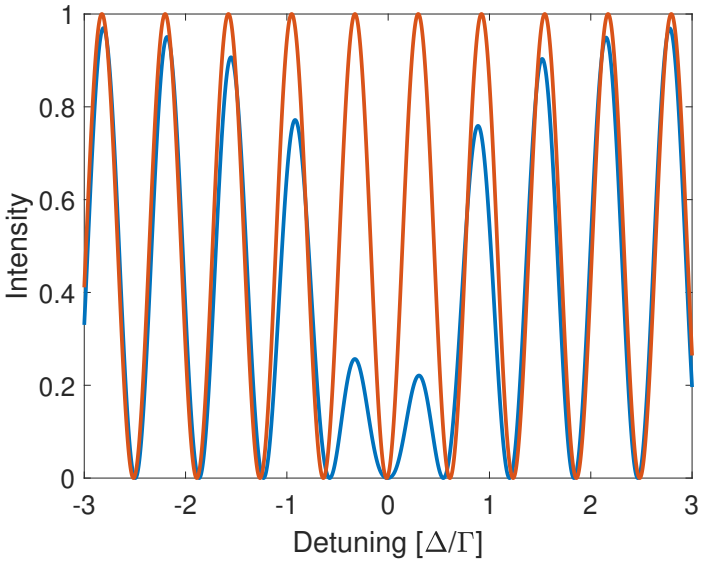

Figure 5.4: Interferometric signal across resonance for QD tuned on(Blue) and off(Orange).

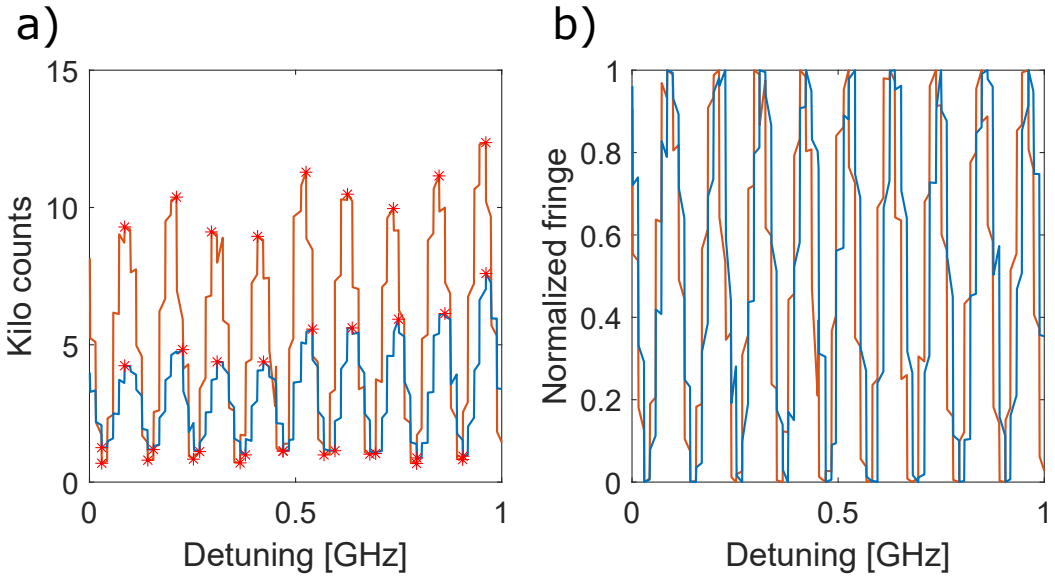

Figure 5.5: a) The interferometric fringe signal for on and off QD measurements across resonance frequency. Red points is peak an valley found from the peak algorithm. b) Normalization of the fringe signal in a)

From this data we can infer the phase shift induced by the QD. The phase shift

is calculated as the phase offset between each peak and valley in the fringes data. First an peak finding algorithm is used to find all peaks and valleys in the two data sets, shown as red points in Fig.5.5.a). Then the data is normalized in between the forund peak and valley, see Fig. Fig.5.5.b). The normalized interferometer intensity function $I = \sin(\varphi/2)^2$ is fitted to all points in between peak to peak, and valley to valley. Thereby the phase shift induced by the quantum dot is calculated as the phase difference between the fits with the QD tuned on and off. An example of two fits are shown in Fig.5.6.a) for the phase shift far off-resonant and close to resonance of the most prominent QD extinction.

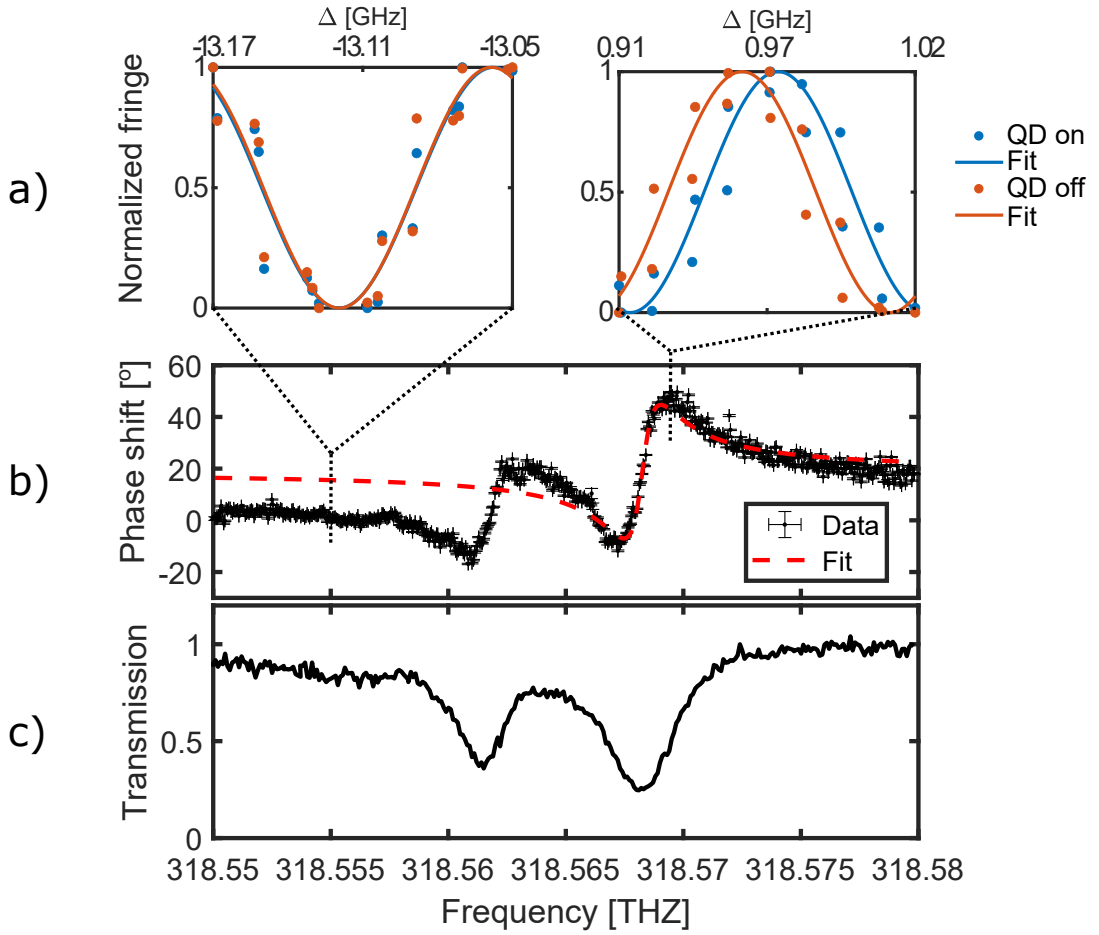

Figure 5.6: a) Example plots of the fit to the fringe signals for the quantum dot tuned on(blue) and off(orange). Corresponding to high and low phaseshift areas indicated by dashed line on b). b) Phase shift measurement result as function of laser frequency along with fit(red) of the theoretical curve. c) Corresponding normalized transmission intensity.

Performing these fits throughout the entire data set we reconstruct the phase shift as function the laser detuning, see Fig. 5.6.b). We observe here a phaseshift at both QD transitions. For the phase shift corresponding to largest transmission dip, we observe from mininmum to maximum a phase range of $58.5[^o] \pm 0.3[^o]$. And if we go off resonance to higher frequencies it a constant offset around $19^o \pm 1^o$ is observed. While at lower frequencies the phase shift goes toward 0^o. It is clear that we have an asymmetry in the phase shift when going across resonance. This might be due to the cavity like behavior as observed in Fig. 5.1, is inducing a Fano resonance like

feature in the signal[21].

5.2.2 Fitting to the theory

Since the transmission intensity and the phaseshift depends on many parameters it can be suitable to fix some parameters when fitting if possible. Here the experimental setup was expanded to measure decay rate of the QD. To do this the QD was excited via another higher energetic transition with a pulsed 910 nm laser. After excitation with the pulse, the fluorescence from the QD was collected from the sample output grating, where fluorescence was measured with a single photon detector. The decay rate of the QD was then measured by tracking the time between excitation and an event on the detector, thus directly giving the lifetime of the QD excitation. The result for this measurement on the given QD is shown in Fig.5.7.

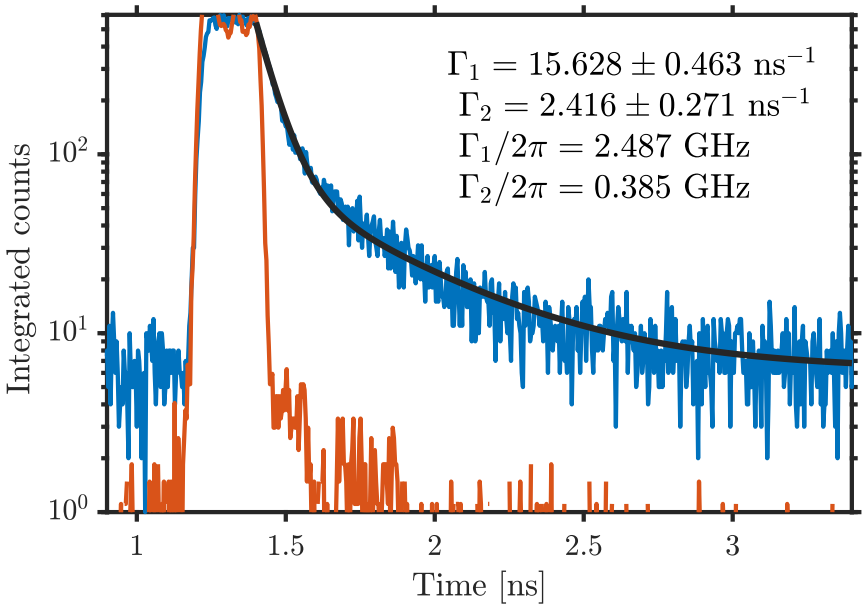

Figure 5.7: Integration of the QD fluorescent(blue) events in time after initial excitation. The double exponential function in black is fitted to obtain the lifetime and decay rate showed in inset text. Orange data is background light.

The data shows two overlapped decays. To make up for this, a double exponential function have been fitted to extract both decays. The one corresponding to the natural linewidth of the QD is $\Gamma_0 = \Gamma_1/2\pi = 2.487GHz$. With this result we can go to fitting the theory for the phase shift and transmission intensity. Since they both dependent on the same parameters they can be fitted dependently.

Fitting to the data presented around the large extinction dip in Fig. 5.6, we obtain the fitting results as shown in Fig. 5.8

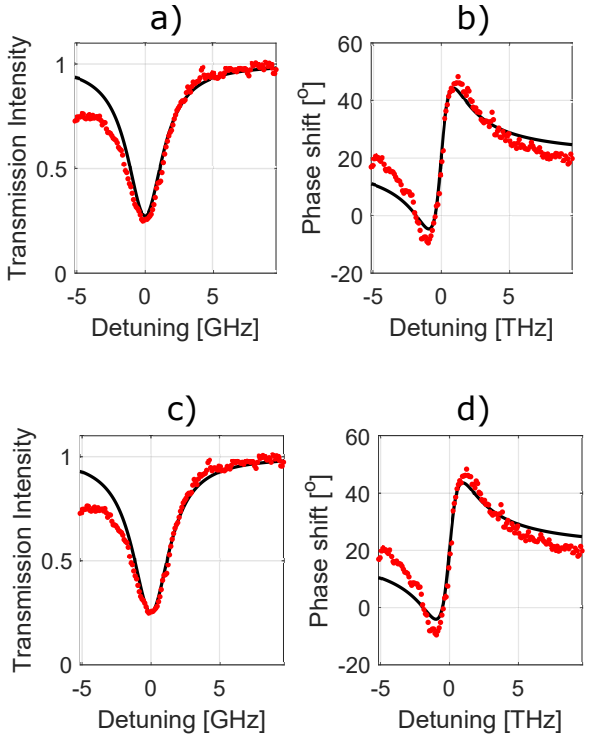

Figure 5.8: a) and b) Shows the dependent fit of the transmission and phase when constraining the natural linewidth. c) and d) Shows the dependent fit of the transmission and phase when keeping fit parameters free.

For the fits in a) and b) the natural line width is fixed to that obtained from Fig.5.7. While in c) and d) no constraint was applied to the fit parameters. We can in both cases see that the fits follows the data quite well. This an indication that the phase shift measurement is able to reproduce data comparable to that of the usual transmission measurement. From the fitting we can try to extract the physical dependent parameters. When fixing the life we obtain:

Fit parameters when fixed to $\Gamma_0 = 2.487$	
$\beta = 0.79 \pm 0.04$	$\nu_{qd} = 318.56821\text{THz} \pm 200\text{MHz}$
$\Gamma_{deph} = 379\text{MHz} \pm 60\text{MHz}$	$\varphi_0 = 19.79^o \pm 0.36^o$

If all the fit parameters instead are kept free, we obtain.

Fit parameters kept free	
$\beta = 0.72 \pm 0.06$	$\nu_{qd} = 318.56821\text{THz} \pm 200\text{MHz}$
$\Gamma_{deph} = 310\text{MHz} \pm 93\text{MHz}$	$\varphi_0 = 19.71^o \pm 0.36^o$
$\Gamma_0 = 2.682\text{GHz} \pm 120\text{MHz}$	

Where Γ_0 is the natural linewidth, Γ_{deph} is the pure dephasing rate. β is the isotropic coupling value. ν_{QD} is the resonance frequency of the quantum dot. Finally in order to compensate for the phase offset the parameter φ_0 is defined as a constant offset.

We can see that both fits agree very well on the resonance frequency and the constant phase offset. However when it comes to estimating the beta they show a discrepancy, but within the errors bars of each other. For the linewidth estimate, we can see that the free fitting estimates a larger linewidth than that found from the lifetime measurement. This enable the fit in the fixed case to compensate with a higher dephasing, while still keeping the coupling high. These fits finds a dephasing of approximately $\Gamma_{deph} = 0.11\Gamma_0$ and $\Gamma_{deph} = 15\Gamma_0$ for the free and fixed case respectively. This is high compared to previous findings with dephasing shown to be in the range $[0,02]\Gamma_0$. similarly with the beta that is typically higher.
The compensation between the β factor and dephasing, for the maximum achievable phase shift is visualized in Fig; 5.10

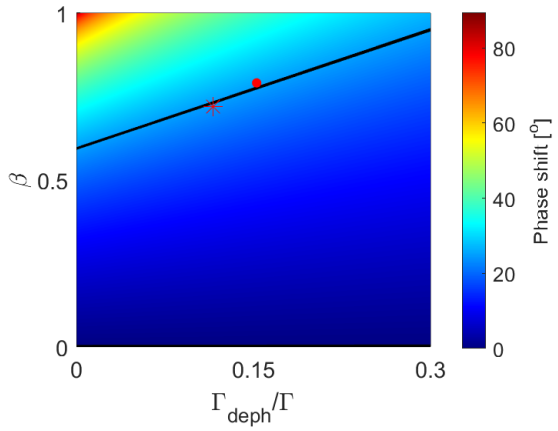

Figure 5.9: Heatmap of maximum measurable phase shift (colorbar). Black line shows 25^o. Result from the fits plotted for free parameter fitting(red Asteriks) and constrained linewidth(red dot).

Here a line of 25^o is plotted on a contour plot of the maximum phase shift as function of β and Γ_{deph}. The 25^o degrees were found as the effective phase shift for the result in Fig 5.6, by comparing peak phase shift to far off resonance. We can see

that both fit results is close to this line, but has however compensated differently for coupling and dephasing.

An earlier measurement of the phase shift induced on transmitted light by a QD, found a maximum phase shift of $\sim 40^o$ with a coupling of $\beta = 0.87$[21]. In comparison to this, we found a maximum phase shift of $\sim 25^o$. When comparing to these results,it is reasonable to expect a lower coupling for this experiment. Which was also found from the fitting. However, the dephasing should not be so significant.

To get a more precise comparison to previous studies additional effects could be taken into account. From the asymmetry observed in the phaseshift measurement in Fig.5.6 it is apparent that the Fano effect could play a role. In addition, spectral diffusion, blinking, and dark transitions.[24][21].

5.2.3 Power dependence of the phase shift

As explored in the theory we saw a high nonlinear dependency on the power. To observe this experimentally, a series of phase shift measurements were at different powers were performed. See Fig. 5.10

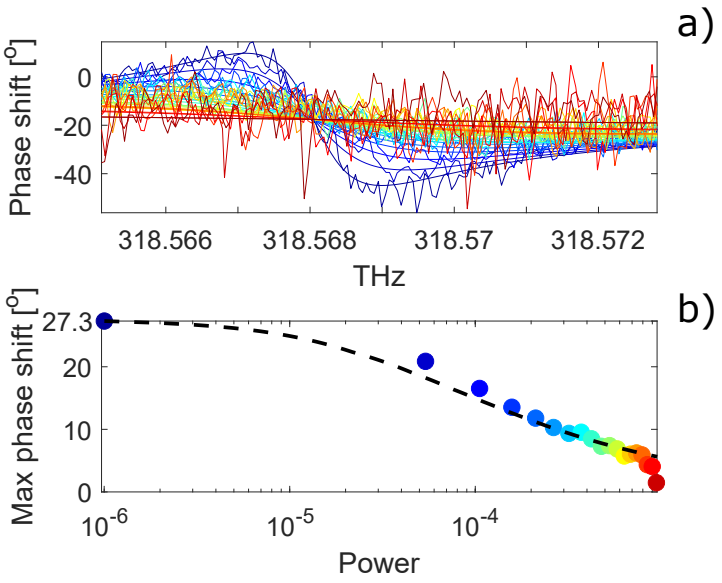

Figure 5.10: a) Phase shift measurements at separate Powers color corresponding to b). b) Maxmimum phase shift from fit in a) as function of power.

We observe here that the data follows the nonlinear behavior of the theory. Fitting the theory of the maximum achieveable phase shift as predicted in chapter

3. We can again give an estimate of the physical values. Using the lifetime as measured in Fig. 5.7, We get two predictions for either with and without fixed Γ_0. When fixing the linewidth we obtain:

$$\beta = 0.79 \qquad \Gamma_0 = 306\text{MHz}$$

And for keeping the fit parameters free

$$\beta = 0.75 \qquad \Gamma_0 = 2.616\text{GHz} \qquad \Gamma_{deph} = 238\text{GHz}$$

First we find that the measured maximum phase shift follow the nonlinear theory explored in chapter 3. For the fits, find that β is comparable to the earlier found in the fits of the phase shift.

From these results we find that using the interferometric method developed we are indeed able to do phase shift measurements that gives comparable results, to that of the normal transmission intensity scans. Additional modeling parameters used in the fitting, might give rise to more literature confident results. However, as we saw in chapter 3 of the theory, chiral coupling is less sensitive to dephasing, thus chiral systems might be more robust in data analysis. Rendering the method of direct phase shift measurement developed in this thesis, more useful.

Chapter 6

Perspective and Conclusion

In this thesis we studied what happens to the phase of light field when coupled to single emitter in a waveguide. From the theory derived in chapter 3 where it was shown that the transmission intensity and coefficient is subject to giant nonlinearities at the single photon level. In particular, exploring the chiral coupling configuration showed very characteristic features, such as a sharp drop in the maximum phase shift when increasing the power, which could be used for direct measurement of the chiral β. factor. Furthermore, it was explored that chiral coupling could give rise a seemingly instantaneous switch in the phase shift from 180^o to 0^o.
To measure such phase shift an inteferometeric setup was build on top of a crysostat which required it to be stabilized with a PZT mounted mirror and micro controller. A stabilization method for stabilizing at any phase difference was developed. The method showed to be able to stabilize the interferometer with a phase fluctuation down to 23.9^o. Due to the effect from the stabilization light on the QD transition, another method was needed to stabilize the inteferomter, using a lock-in amplifier with a PID loop at low power.This showed to almost stabilize to a similar degree as the previous method with a phase fluctuation of 28.1^o.
By using such the stabilized inerferometer an interferometric fringe signal was measured while sweeping the laser frequency. This approved the stabilization of the interferometer. From this measurement we managed to extract a maximum phase shift of $58.5^o \pm 0.3^o$. when compensating for the constant offset, the fits showed that this correspond to a phase shift of $\sim 25^o$ induced by the single transition. This were shown to be less then the $\sim 40^o$ obtained previously[21].However was in agreement with, that the QD considered here was estimated to have worse coupling and a higher dephasing.

Fitting the obtained phase shift from measurement together with the intensity showed good agreement with theory. Therefore rendering the interferometer a new measurement tool in the lab of equal merit. Furthermore, the nonlinear behavior of

the phase shift, was shown.

The next immediate step with this new tool in the lab, is to achieve a measurement with a cleaner QD transition i.e. without an adjacent QD transition. The experiment could then be expanded into measurements regarding chiral emission, to try and measure the expected π phase shift. This can give proof of and characterize the chiral nature, when the time comes for implementing it in the lab, And finally for bigger circuits when entering the regime of quantum communication an computing.

Additionally the method developed for stabilization of the interferometer can potentially allow stabilization at any phase difference. This can enable the interferometer to be a new measurement tool to perform tomography measurements of the scattered light[41]. This tomography measurement could also be used to examine the scattering of light with different modal structure[19] [18].

Appendix A

Interferometer Stabilization

.

A.1 Parameter Sweep

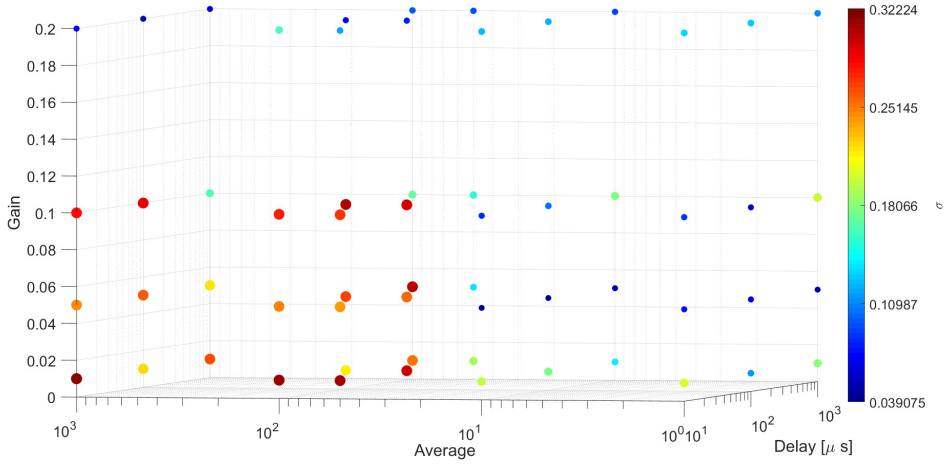

Figure A.1: 3D scatter plot of the parameter sweep of the algorithm values. The standard deviation of the voltage is indicated on the color bar and point size is proportional to it.

A.2 Fluctuations

The mechanical noise was thought to come form a variety of sources. Below we have supplied some measurements of the case where a 50% Hz mechanical noise from the

optical equipment and the effect from the cryostat compressor oscillations.

Fig. A.2 shows a an example of mechanical excitation of the cryostat interferometer and the oscillatory. dampening afterwards.

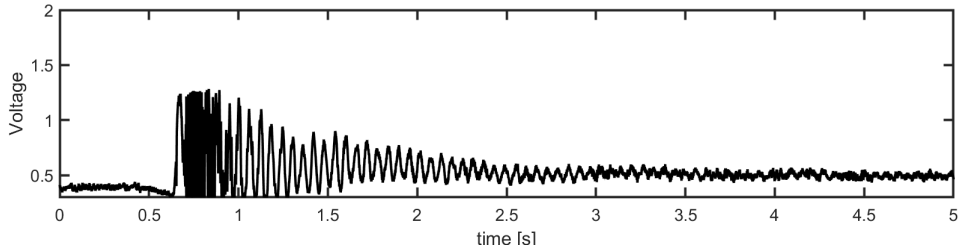

Figure A.2: Time trace the interferometer signal while by passing the cryostat.

The noise in the more stable areas is less noisy as otherwise shown, since the cryostat transmission is bypassed and the inteferometer is kept on the mounting plate.

A.2.1 50 Hz noise

Fig. A.3 shows a time trace of the non stabilized signal while the the optical mouting plate is mounted on rubber spaces.

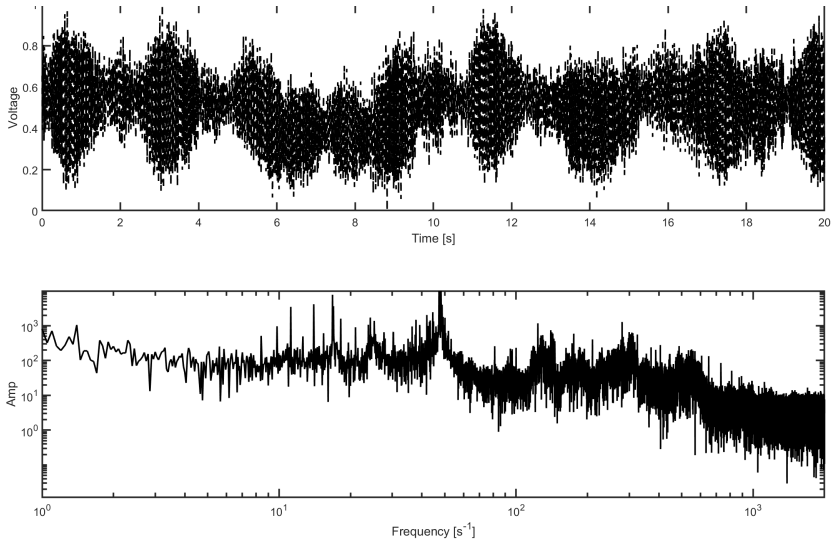

Figure A.3: Time trace of the non-stabilized signal(*top*) along with the fourier transform of he signal below(*bottom*).

A prominent signal is observable close to the 50 Hz signal. While observing this spectrum when removing some equipment this peak, was found to tune. Thus indicating that the noise was of mechanical acoustic origin.

As evident from Fig.A.4, running the stabilizing code on the Arduino, did not seem to be able to remove the 50 HZ noise. Though other frequencies seem to be dampened, perhaps indicating the that the 50 Hz fluctuations is physically larger than the expansion range of the PZT.

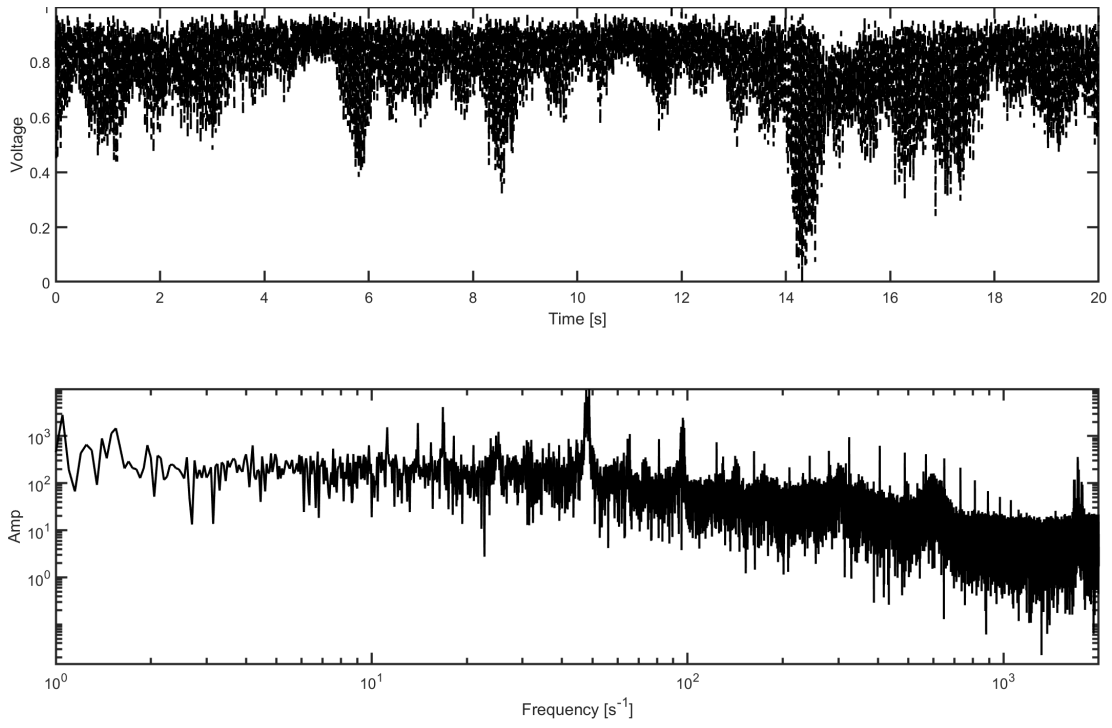

Figure A.4: Time trace of the stabilized interferometer output (top) compared the fourier transform(bottom)

A.2.2 Cyrostat Compressor noise

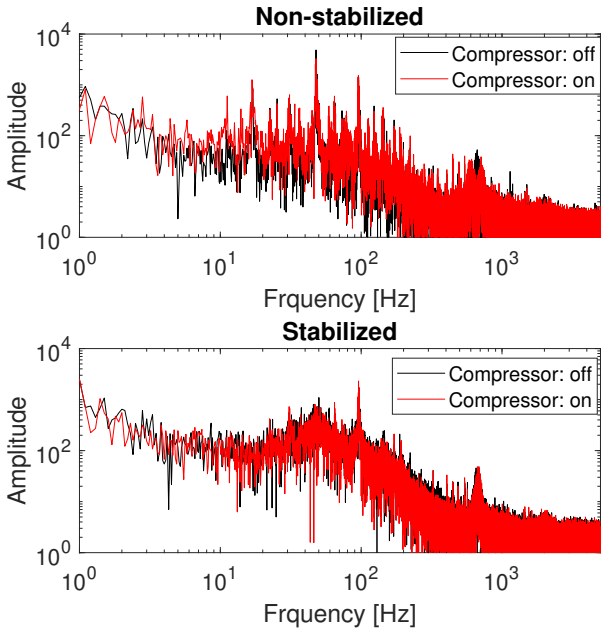

Figure A.5: Spectrum of the interferometer while turning the compressor on(red) and off(black). For the stabilized and non-stabilized signal.

A.2.3 Power Stabilization instabillity

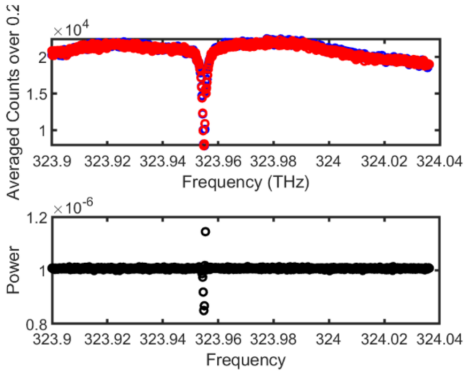

Figure A.6: A scan of the measured counts vs input power.The dip in power made it look like a QD transition were found.

Fluctuations in the power gave rise to signals that looked like quantum dots.

A.3 Amplifier

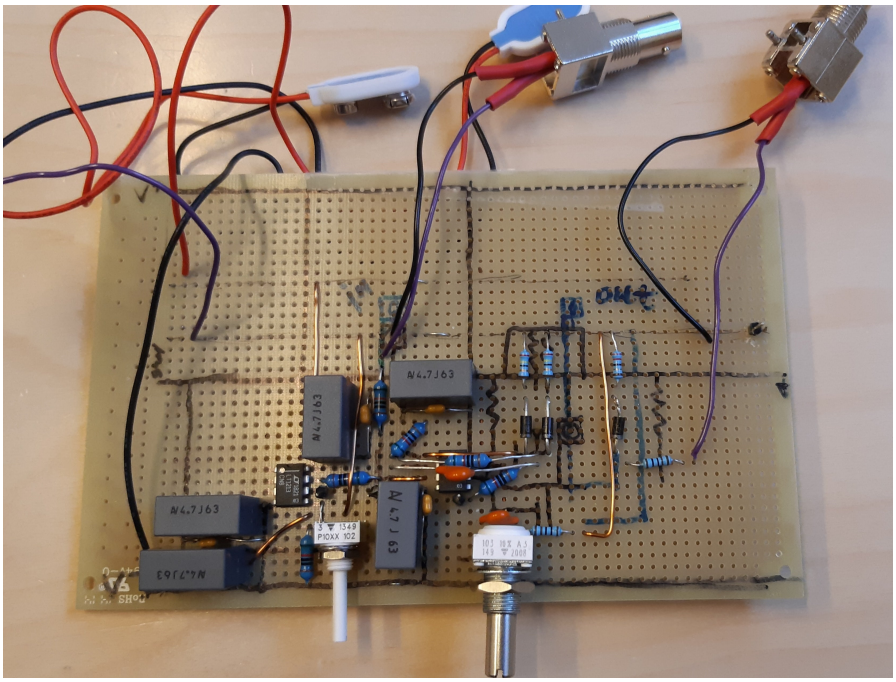

Figure A.7: Picture of the build amplifier circuit in Fig. 4.15

A.4 Power dependency

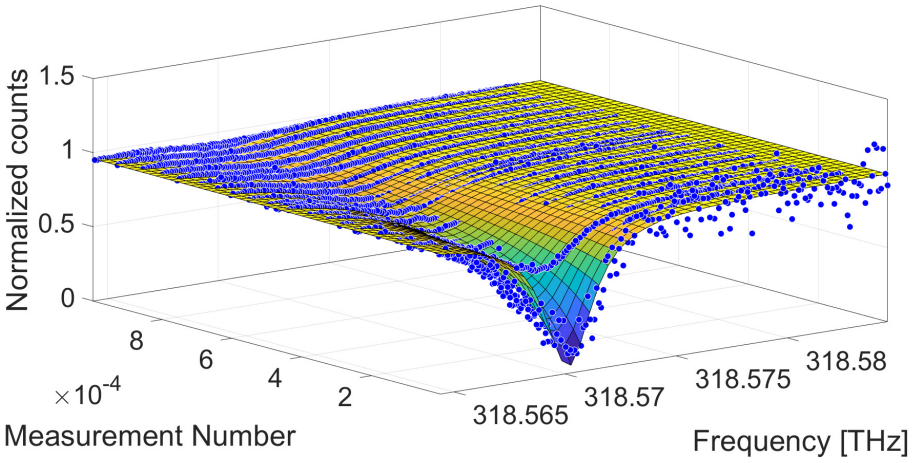

Figure A.8: Power series of transmission with fit

This power series correspond to a saturation of the transmission extinction at zero detuning. A.9.

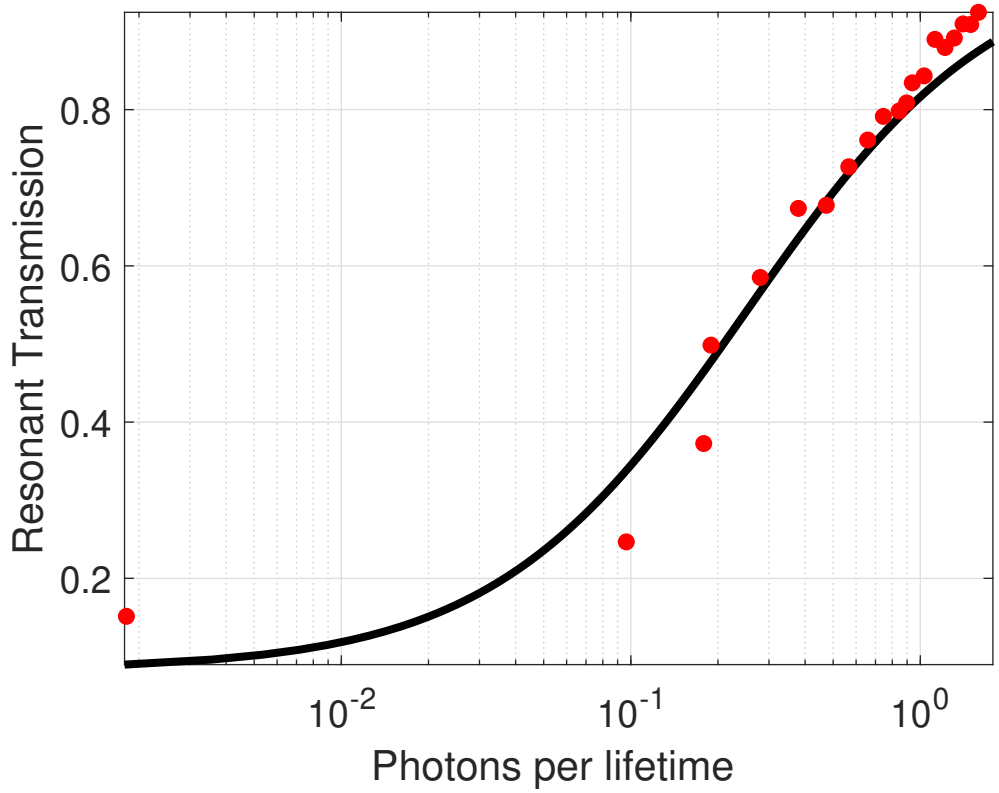

Figure A.9: Saturation curve of transmission at resonance(red) with fitted theory (black)

Here we see a saturation of the QD interaction, from the increasing transmission at QD resonance. By fitting the series of transmission measurement at different power (Appendix). From these fits coupling factor is found to $\beta = 0.72$, while keeping the natural linewidth and dephasing as free parameters. However fixing the linewidth to that of measured in lifetime measurements, retrieve $\beta \sim 1$. Which is a huge difference.

Bibliography

[1] Syed Abdullah Aljunid et al. "Phase Shift of a Weak Coherent Beam Induced by a Single Atom". In: *Physical Review Letters* 103.15 (Oct. 2009). ISSN: 1079-7114. DOI: 10.1103/physrevlett.103.153601. URL: http://dx.doi.org/10.1103/PhysRevLett.103.153601.

[2] M. Arcari et al. "Near-Unity Coupling Efficiency of a Quantum Emitter to a Photonic Crystal Waveguide". In: *Phys. Rev. Lett.* 113 (9 Aug. 2014), p. 093603. DOI: 10.1103/PhysRevLett.113.093603. URL: https://link.aps.org/doi/10.1103/PhysRevLett.113.093603.

[3] *Arduino Due*. 2021. URL: https://store.arduino.cc/arduino-due (visited on 04/13/2021).

[4] A. Asenjo-Garcia et al. "Atom-light interactions in quasi-one-dimensional nanostructures: A Green's-function perspective". In: *Phys. Rev. A* 95 (3 Mar. 2017), p. 033818. DOI: 10.1103/PhysRevA.95.033818. URL: https://link.aps.org/doi/10.1103/PhysRevA.95.033818.

[5] Alexia Auffèves-Garnier et al. "Giant optical nonlinearity induced by a single two-level system interacting with a cavity in the Purcell regime". In: *Phys. Rev. A* 75 (5 May 2007), p. 053823. DOI: 10.1103/PhysRevA.75.053823. URL: https://link.aps.org/doi/10.1103/PhysRevA.75.053823.

[6] J. Borregaard, A. S. Sørensen, and P. Lodahl. *Quantum Networks with Deterministic Spin-Photon Interfaces*. 2019. arXiv: 1811.08242 [quant-ph].

[7] Stefan Yosih Buhmann. *Dispersion forces*. Springer, 2012. ISBN: 978-3-642-32483-3. DOI: 10.1007/978-3-642-32484-0.

[8] Darrick E. Chang, Vladan Vuletić, and Mikhail D. Lukin. "Quantum nonlinear optics — photon by photon". In: *Nature Photonics* 8.9 (Sept. 2014), pp. 685–694. ISSN: 1749-4893. DOI: 10.1038/nphoton.2014.192. URL: https://doi.org/10.1038/nphoton.2014.192.

[9] Isaac L. Chuang and Yoshihisa Yamamoto. "Simple quantum computer". In: *Phys. Rev. A* 52 (5 Nov. 1995), pp. 3489–3496. DOI: 10.1103/PhysRevA.52.3489. URL: https://link.aps.org/doi/10.1103/PhysRevA.52.3489.

[10] J. Ignacio Cirac and Peter Zoller. "Goals and opportunities in quantum simulation". In: *Nature Physics* 8.4 (Apr. 2012), pp. 264–266. ISSN: 1745-2481. DOI: 10.1038/nphys2275. URL: https://doi.org/10.1038/nphys2275.

[11] Amir Feizpour et al. "Observation of the nonlinear phase shift due to single post-selected photons". In: *Nature Physics* 11.11 (Nov. 2015), pp. 905–909. ISSN: 1745-2481. DOI: 10.1038/nphys3433. URL: https://doi.org/10.1038/nphys3433.

[12] Martin Fischer et al. "Shifting the phase of a coherent beam with a

$$^{174}\mathrm{Yb}^{+}$$

174 Yb + ion: influence of the scattering cross section". In: *Applied Physics B* 123.1 (Jan. 2017). ISSN: 1432-0649. DOI: 10.1007/s00340-016-6609-3. URL: http://dx.doi.org/10.1007/s00340-016-6609-3.

[13] A. P. Foster et al. "Tunable Photon Statistics Exploiting the Fano Effect in a Waveguide". In: *Physical Review Letters* 122.17 (May 2019). ISSN: 1079-7114. DOI: 10.1103/physrevlett.122.173603. URL: http://dx.doi.org/10.1103/PhysRevLett.122.173603.

[14] Ilya Fushman et al. "Controlled Phase Shifts with a Single Quantum Dot". In: *Science* 320.5877 (2008), pp. 769–772. ISSN: 0036-8075. DOI: 10.1126/science.1154643. eprint: https://science.sciencemag.org/content/320/5877/769.full.pdf. URL: https://science.sciencemag.org/content/320/5877/769.

[15] Christopher Gerry and Peter Knight. *Introductory Quantum Optics*. Cambridge University Press, 2004. DOI: 10.1017/CBO9780511791239.

[16] K. Hennessy et al. "Quantum nature of a strongly coupled single quantum dot–cavity system". In: *Nature* 445.7130 (Feb. 2007), pp. 896–899. ISSN: 1476-4687. DOI: 10.1038/nature05586. URL: https://doi.org/10.1038/nature05586.

[17] K. Huang et al. "Microcontroller-based locking in optics experiments". In: *Review of Scientific Instruments* 85.12 (2014), p. 123112. DOI: 10.1063/1.4903869. eprint: https://doi.org/10.1063/1.4903869. URL: https://doi.org/10.1063/1.4903869.

[18] Alexander Holm Kiilerich and Klaus Mølmer. "Input-Output Theory with Quantum Pulses". In: *Phys. Rev. Lett.* 123 (12 Sept. 2019), p. 123604. DOI: 10.1103/PhysRevLett.123.123604. URL: https://link.aps.org/doi/10.1103/PhysRevLett.123.123604.

[19] Alexander Holm Kiilerich and Klaus Mølmer. "Quantum interactions with pulses of radiation". In: *Phys. Rev. A* 102 (2 Aug. 2020), p. 023717. DOI: 10.1103/PhysRevA.102.023717. URL: https://link.aps.org/doi/10.1103/PhysRevA.102.023717.

[20] H. J. Kimble. "The quantum internet". In: *Nature* 453.7198 (June 2008), pp. 1023–1030. ISSN: 1476-4687. DOI: 10.1038/nature07127. URL: https://doi.org/10.1038/nature07127.

[21] Hanna Le Jeannic et al. "Experimental Reconstruction of the Few-Photon Nonlinear Scattering Matrix from a Single Quantum Dot in a Nanophotonic Waveguide". In: *Phys. Rev. Lett.* 126 (2 Jan. 2021), p. 023603. DOI: 10.1103/PhysRevLett.126.023603. URL: https://link.aps.org/doi/10.1103/PhysRevLett.126.023603.

[22] Daniel Llewellyn et al. "Chip-to-chip quantum teleportation and multi-photon entanglement in silicon". In: *Nature Physics* 16.2 (Feb. 2020), pp. 148–153. ISSN: 1745-2481. DOI: 10.1038/s41567-019-0727-x. URL: https://doi.org/10.1038/s41567-019-0727-x.

[23] Peter Lodahl. "Quantum-dot based photonic quantum networks". In: *Quantum Science and Technology* 3.1 (Oct. 2017), p. 013001. DOI: 10.1088/2058-9565/aa91bb. URL: https://doi.org/10.1088/2058-9565/aa91bb.

[24] Peter Lodahl, Sahand Mahmoodian, and Søren Stobbe. "Interfacing single photons and single quantum dots with photonic nanostructures". In: *Rev. Mod. Phys.* 87 (2 May 2015), pp. 347–400. DOI: 10.1103/RevModPhys.87.347. URL: https://link.aps.org/doi/10.1103/RevModPhys.87.347.

[25] Peter Lodahl et al. "Chiral quantum optics". In: *Nature* 541.7638 (Jan. 2017), pp. 473–480. ISSN: 1476-4687. DOI: 10.1038/nature21037. URL: https://doi.org/10.1038/nature21037.

[26] Peter Lodahl et al. "Controlling the dynamics of spontaneous emission from quantum dots by photonic crystals". In: *Nature* 430.7000 (Aug. 2004), pp. 654–657. ISSN: 1476-4687. DOI: 10.1038/nature02772. URL: https://doi.org/10.1038/nature02772.

[27] Marcelo Alejandro Luda et al. "Compact embedded device for lock-in measurements and experiment active control". In: *Review of Scientific Instruments* 90.2 (2019), p. 023106. DOI: 10.1063/1.5080345. eprint: https://doi.org/10.1063/1.5080345. URL: https://doi.org/10.1063/1.5080345.

[28] Sahand Mahmoodian, Peter Lodahl, and Anders S. Sørensen. "Quantum Networks with Chiral-Light–Matter Interaction in Waveguides". In: *Phys. Rev. Lett.* 117 (24 Dec. 2016), p. 240501. DOI: 10.1103/PhysRevLett.117.240501. URL: https://link.aps.org/doi/10.1103/PhysRevLett.117.240501.

[29] Pierre Meystre and Murray Sargent. *Elements of Quantum Optics, Fourth Edition*. Springer, 2007. ISBN: 9783540742098.

[30] L Midolo et al. "Soft-mask fabrication of gallium arsenide nanomembranes for integrated quantum photonics". In: *Nanotechnology* 26.48 (Nov. 2015), p. 484002. DOI: 10.1088/0957-4484/26/48/484002. URL: https://doi.org/10.1088/0957-4484/26/48/484002.

[31] Michael A. Nielsen and Isaac L. Chuang. *Quantum Computation and Quantum Information: 10th Anniversary Edition*. Cambridge University Press, 2010. DOI: 10.1017/CBO9780511976667.

[32] Lukas Novotny and Bert Hecht. *Principles of nano-optics*. Cambridge University Press, 2006. ISBN: 9780521832243.

[33] Freja T. Pedersen et al. *Near Transform-limited Quantum Dot Linewidths in a Broadband Photonic Crystal Waveguide*. 2020. arXiv: 2005.03943 [quant-ph].

[34] Adi Pick et al. *Boosting photonic quantum computation with moderate nonlinearity*. 2021. arXiv: 2011.06454 [quant-ph].

[35] Alberto Politi et al. "Silica-on-Silicon Waveguide Quantum Circuits". In: *Science* 320.5876 (2008), pp. 646–649. ISSN: 0036-8075. DOI: 10.1126/science.1155441. eprint: https://science.sciencemag.org/content/320/5876/646.full.pdf. URL: https://science.sciencemag.org/content/320/5876/646.

[36] Eugene S. Polzik and Jaromír Fiurášek. "Quantum Interface Between Light and Atomic Ensembles". In: *Quantum Information*. John Wiley Sons, Ltd, 2016. Chap. 31, pp. 701–722. ISBN: 9783527805785. DOI: https://doi.org/10.1002/9783527805785.ch31. eprint: https://onlinelibrary.wiley.com/doi/pdf/10.1002/9783527805785.ch31. URL: https://onlinelibrary.wiley.com/doi/abs/10.1002/9783527805785.ch31.

[37] M. Pototschnig et al. "Controlling the Phase of a Light Beam with a Single Molecule". In: *Phys. Rev. Lett.* 107 (6 Aug. 2011), p. 063001. DOI: 10.1103/PhysRevLett.107.063001. URL: https://link.aps.org/doi/10.1103/PhysRevLett.107.063001.

[38] T. Pregnolato et al. "Deterministic positioning of nanophotonic waveguides around single self-assembled quantum dots". In: *APL Photonics* 5.8 (2020), p. 086101. DOI: 10.1063/1.5117888. eprint: https://doi.org/10.1063/1.5117888. URL: https://doi.org/10.1063/1.5117888.

[39] *Red Pitaya-14*. 2021. URL: https://www.redpitaya.com/f130/STEMlab-board (visited on 04/13/2021).

[40] C. Sames et al. “Antiresonance Phase Shift in Strongly Coupled Cavity QED”. In: *Physical Review Letters* 112.4 (Jan. 2014). ISSN: 1079-7114. DOI: 10.1103/physrevlett.112.043601. URL: http://dx.doi.org/10.1103/PhysRevLett.112.043601.

[41] Carsten H. H. Schulte et al. “Quadrature squeezed photons from a two-level system”. In: *Nature* 525.7568 (Sept. 2015), pp. 222–225. ISSN: 1476-4687. DOI: 10.1038/nature14868. URL: https://doi.org/10.1038/nature14868.

[42] Steven H. Simon. *The Oxford Solid States Basiscs*. Oxford University Press 2016, 2013. ISBN: 9780199680764.

[43] Signe Folden Simonsen. “nderstanding nonlinearities in a photonic crystal waveguide with a quantum dot”. PhD thesis. University of Copenhagen, 2019, p. 78.

[44] Immo Söllner et al. “Deterministic photon–emitter coupling in chiral photonic circuits”. In: *Nature Nanotechnology* 10.9 (Sept. 2015), pp. 775–778. ISSN: 1748-3395. DOI: 10.1038/nnano.2015.159. URL: https://doi.org/10.1038/nnano.2015.159.

[45] Henri Thyrrestrup et al. “Quantum Optics with Near-Lifetime-Limited Quantum-Dot Transitions in a Nanophotonic Waveguide”. In: *Nano Letters* 18.3 (Mar. 2018), pp. 1801–1806. ISSN: 1530-6984. DOI: 10.1021/acs.nanolett.7b05016. URL: https://doi.org/10.1021/acs.nanolett.7b05016.

[46] Q. A. Turchette et al. “Measurement of Conditional Phase Shifts for Quantum Logic”. In: *Phys. Rev. Lett.* 75 (25 Dec. 1995), pp. 4710–4713. DOI: 10.1103/PhysRevLett.75.4710. URL: https://link.aps.org/doi/10.1103/PhysRevLett.75.4710.

[47] Pierre Türschmann et al. “Coherent nonlinear optics of quantum emitters in nanophotonic waveguides”. In: *Nanophotonics* 8.10 (2019), pp. 1641–1657. DOI: doi:10.1515/nanoph-2019-0126. URL: https://doi.org/10.1515/nanoph-2019-0126.

[48] Ravitej Uppu et al. “Scalable integrated single-photon source”. In: *Science Advances* 6.50 (2020). DOI: 10.1126/sciadv.abc8268. eprint: https://advances.sciencemag.org/content/6/50/eabc8268.full.pdf. URL: https://advances.sciencemag.org/content/6/50/eabc8268.

[49] L.M. Wells et al. “Photon Phase Shift at the Few-Photon Level and Optical Switching by a Quantum Dot in a Microcavity”. In: *Phys. Rev. Applied* 11 (6 June 2019), p. 061001. DOI: 10.1103/PhysRevApplied.11.061001. URL: https://link.aps.org/doi/10.1103/PhysRevApplied.11.061001.

[50] A. B. Young et al. “Quantum-dot-induced phase shift in a pillar microcavity”. In: *Phys. Rev. A* 84 (1 July 2011), p. 011803. DOI: 10.1103/PhysRevA.84.011803. URL: https://link.aps.org/doi/10.1103/PhysRevA.84.011803.

[51] A. S. Zibrov et al. “Experimental Demonstration of Enhanced Index of Refraction via Quantum Coherence in Rb”. In: *Phys. Rev. Lett.* 76 (21 May 1996), pp. 3935–3938. DOI: 10.1103/PhysRevLett.76.3935. URL: https://link.aps.org/doi/10.1103/PhysRevLett.76.3935.